

The micro-structure of the intergalactic medium I: the 21cm signature from dynamical minihaloes

Avery Meiksin

*SUPA**, *Institute for Astronomy, University of Edinburgh, Blackford Hill, Edinburgh EH9 3HJ, UK*

15 April 2019

ABSTRACT

A unified description is provided for the 21cm signatures arising from minihaloes against a bright background radio source and against the Cosmic Microwave Background (CMB), within the context of a dynamical collapsing cosmological spherical halo. The effects of gas cooling via radiative atomic and molecular processes and of star formation on setting the maximum mass of the minihaloes giving rise to a 21cm signal are included. Models are computed both with and without molecular hydrogen formation, allowing for its possible suppression by an ambient ultra-violet radiation field. The spectral signatures and equivalent width distributions are computed for a Λ CDM cosmology. The brightness temperature differential relative to the CMB is also computed. The effects of an ambient $\text{Ly}\alpha$ radiation field and heating of the IGM on the signatures are also examined.

Degeneracies in the strengths of the predicted signals are found, depending on the spectral index of the primordial power spectrum, the intensity of the ambient $\text{Ly}\alpha$ radiation field, and the amount of heating of the IGM. It is shown that within current observational constraints, a running spectral index could suppress the signals by as much as an order of magnitude. Under some circumstances, the degeneracies may be removed by combining the absorption signal against bright background radio sources with the signal against the CMB. Heating weakens the absorption signal against a bright radio source whilst strengthening the emission signal against the CMB if the IGM is heated to a temperature above that of the CMB. In the absence of heating, a $\text{Ly}\alpha$ photon scattering rate approaching the thermalization rate increases the number of absorption systems against a bright background radio source by more than two orders of magnitude. It can also give rise to mock emission lines relative to the broad absorption wings produced by the diffuse IGM. In the absence of IGM heating, a $\text{Ly}\alpha$ photon scattering rate as small as one percent of the thermalization rate produces a net absorption signal against the CMB from the region surrounding the minihaloes that swamps the emission signal produced by the minihalo cores. If the IGM is heated to a temperature above that of the CMB, then the emission signal from the surrounding gas swamps that of the minihalo core even without any $\text{Ly}\alpha$ photon scattering. There is thus a very narrow range of parameters for which an emission signature from minihaloes against the CMB would be detectable.

Key words: atomic processes – cosmology: theory – line: formation – radio lines: general

1 INTRODUCTION

A principal science goal of the Square Kilometre Array (SKA)¹ is the detection of neutral hydrogen in the Intergalactic Medium (IGM) following the recombination epoch and prior to the Epoch of Reionization (EoR), performing

3D tomography of the filamentary large scale structure of the Universe as revealed by neutral hydrogen at the end of the Dark Ages when the first sources of light emerge in the Universe after the Big Bang (Hogan & Rees 1979; Scott & Rees 1990; Madau et al. 1997). Even before SKA is built, the absorption of a still largely neutral IGM may be detectable against radio loud galaxies or quasars by SKA

* Scottish Universities Physics Alliance

¹ www.skatelescope.org

pathfinders like the LOw Frequency ARray (LOFAR)² and the Long Wavelength Array (LWA)³, both already underway, and the Murchison Widefield Array (MWA)⁴, a SKA precursor facility soon to start.

Extracting the EoR signal from the radio data is a major undertaking requiring modelling of both the expected 21cm signature and the effects of contaminating sources which will swamp the underlying cosmological signal (Hogan & Rees 1979; Shaver et al. 1999; Morales et al. 2006; Jelić et al. 2008). The extraction of the EoR signature is further complicated by uncertainties in the signature itself arising from the unknown manner in which the Universe was reionized and from the structure of the IGM. The 21cm signals will be highly patchy, as the cold hydrogen atoms will closely trace the filamentary structure of the dark matter in the Universe on large scales and the non-linear fluctuations in the dark matter on the very small. If a bright background radio source is present, the intervening neutral hydrogen in the IGM will produce an absorption signature against it, with a strength depending on the temperature of the IGM and how efficiently the spin temperature is coupled to it (Field 1959a). The IGM will also produce a fluctuating signal against the Cosmic Microwave Background (CMB) (Hogan & Rees 1979; Scott & Rees 1990; Tozzi et al. 2000), either in absorption or emission depending on the gas kinetic temperature compared with the CMB temperature. Only on scales small compared with the Jeans length of the gas will the IGM produce a smooth signal. The neutral hydrogen thus provides a unique means of measuring the power spectrum of dark matter over a wide range of length scales spanning six decades at the as yet unprobed epochs between the Recombination Era and the emergence of the first galaxies.

Perhaps the best prospects for detecting a still neutral IGM is in absorption against a bright background radio source. Collapsed minihaloes will produce a 21-cm forest of absorption features in the radio spectrum of such a source (Carilli et al. 2002; Furlanetto & Loeb 2002). Whilst this will be superposed on a global absorption signature arising from the diffuse IGM, the deeper absorption features may be more amenable to a clean detection than the signal against the CMB by an instrument able to resolve the minihalo signature in frequency.

The detection of the 21cm signature against the CMB requires that the hyperfine spin structure of the hydrogen be decoupled from the CMB. The signal will consequently reflect the processes which achieve the decoupling in addition to the spatial distribution of the gas. Two mechanisms dominate: collisional decoupling through collisions with electrons and other hydrogen atoms, and decoupling resulting from the scattering of Ly α (and other Lyman resonance line) photons through the Wouthuysen-Field effect (Wouthuysen 1952; Field 1958) once a sufficient intensity of Lyman resonance line photons builds up in the IGM from the first stars and galaxies.

Even without an adequate supply of Lyman resonance line photons, collisions provide a sufficient means of coupling the spin temperature to the gas temperature in virialised

structures at $z > 6$ (Madau et al. 1997). It was argued by Ilev et al. (2002) that minihaloes will produce a substantial signal against the CMB at $z > 6$, and will dominate over the diffuse IGM before an adequate flux of Ly α photons develops to decouple the spin temperature of the diffuse IGM from the CMB temperature. This has been disputed by Oh & Mack (2003), who objected that, because of the overwhelming amount of mass in the diffuse IGM compared with minihaloes, except very early on before there is any feedback from galaxies, the diffuse component will dominate. Numerical simulations have tended to confirm this expectation (Kuhlen et al. 2006; Yue et al. 2009). Using an extension of the Press-Schechter formalism, Furlanetto & Loeb (2004) suggested that even without galactic feedback, the 21cm signal from the shocked diffuse IGM would exceed that due to the minihaloes. High spatial resolution numerical simulations by Kuhlen et al. (2006) appear to confirm this claim, although the opposing view has again been defended by Shapiro et al. (2006).

Estimates of the strength of the 21cm signature from minihaloes are made uncertain by several poorly known factors. The number density of the haloes is notoriously difficult to quantify, especially since the minihaloes arise on scales for which the dark matter power spectrum is approaching the “flicker noise” small-scale limit, for which structures on all scales collapse and virialise simultaneously. Numerical simulations are currently not of much help for estimating the distribution of dark matter haloes or their internal structure on all the relevant scales, as it is not yet possible to capture the power over the full dynamic range required.

Another uncertainty is the mass range of minihaloes which contribute to the 21cm signature. It is generally assumed halo masses below the Jeans mass of the IGM will contribute negligibly, while more massive haloes will produce a 21cm signature up to halo masses with a limiting virial temperature near 10^4 K, above which the collapsing gas will cool through the collisional excitation of hydrogen and make stars. As will be shown, one consequence of allowing for the dynamics of the collapsing haloes is a modification of the mass range. Haloes below the Jeans mass contribute non-negligibly, whilst the upper mass limit may correspond to haloes with virial temperatures below 10^4 K before either atomic or molecular radiative losses become sufficiently efficient to produce a cooling runaway and an adequate amount of star formation to lead to the ejection of gas from the haloes.

In previous models, the minihaloes have generally been assumed to be isothermal and in hydrostatic equilibrium. It was recognised in the context of the minihalo model for Ly α forest absorption systems (Ikeuchi 1986; Rees 1986), that the systems will in general be formed in dynamically collapsing (Bond et al. 1988) and non-isothermal (Meiksin 1994) dark matter haloes. Allowing for the dynamics introduces modifications to the thermal structure and pressure support of the gas in the minihaloes, which in turn modify the cross sections for their detection.

The primary purpose of this paper is to address the effect of some of these assumptions and uncertainties on the expected 21cm signatures from minihaloes. The haloes are evolved as spherical density perturbations. Treating the haloes as arising from isolated perturbations is itself an approximation, as in bottom-up scenarios like cold dark mat-

² www.lofar.org

³ wa.phys.unm.edu

⁴ www.mwatelescope.org

ter dominated cosmologies, structures are created from the merger of smaller systems. In this sense, the perturbations are more representative of an evolving patch of smaller haloes which merge into the final collapsed structure. In the early stages of evolution, even this is not a good approximation as the overdense patches are typically triaxial (Bardeen et al. 1986), but as an overdense region approaches its collapse epoch it becomes increasingly spherical.

The collapsing spherical halo approximation has the advantage over the static isothermal halo approximation of allowing the density and temperature profiles to arise naturally during the collapse of the halo. The modelling of an evolving system also reveals some of the dynamical effects which may play an important role in the cooling of the gas and in determining the minimum halo mass at which star formation sets in. It is argued that only a small number of stars need form before the remaining gas in the minihalo will be expelled through mechanical feedback due to photo-evaporative winds and supernovae. The formation of molecular hydrogen is computed and the rate of star formation modelled to provide an estimate for the upper limiting minihalo mass at any given collapse epoch. (More massive systems than minihaloes become increasingly complex, such as forming galaxy haloes and their associated discs, and are not considered here.) The effect of a radiation field sufficiently intense to suppress H_2 gas-phase formation processes and subsequent star formation and halo disruption is also explored.

Only the 21cm signal from fully collapsed haloes, along with their surrounding infall regions, is considered in this paper. Extended patches of gas within which no minihaloes sufficiently massive to retain their baryons have collapsed may also contribute to the 21cm signal. The treatment of such patches is deferred to a later work, although comparison is made with the total signal that could potentially arise from a diffuse homogeneous component. Ultimately a very high resolution fully 3D combined dark matter and hydrodynamics simulation would be required for a precise prediction of the expected 21cm signatures.

A second purpose of this paper is to provide a semi-analytic framework that incorporates the dynamical effects to estimate the 21cm signals from minihaloes. Numerical simulations are still unable to resolve the full range of scales required to estimate the 21cm signature without some semi-analytic modelling, and even if they were able to do so, they are very costly to run. Alternative halo mass distributions may be readily explored within the semi-analytic framework. The 21cm signatures produced by minihaloes also probe a part of the cosmological dark matter power spectrum that has never been measured at high redshifts, down to scales on the order of a comoving kiloparsec, or a millionth of the cosmological horizon. The effect of different cosmological scenarios, such as alterations to the small-scale power spectrum, may be readily examined within the framework. It is demonstrated below that the minihalo 21cm signature may in fact provide a useful means for distinguishing between rival predictions for the amount of power on small scales.

Unless stated otherwise, the present-day values of the cosmological parameters assumed are $\Omega_M = 0.27$, $\Omega_v = 0.73$, $\Omega_b = 0.0456$, $h = 0.70$, $\sigma_{8h^{-1}} = 0.81$ and $n = 0.96$ for the total mass, vacuum energy and baryon density parameters, the Hubble constant ($h = H_0/100 \text{ km s}^{-1} \text{ Mpc}^{-1}$),

the linear density fluctuation amplitude on a scale of $8h^{-1} \text{ Mpc}$ and the spectral index, respectively, consistent with CMB measurements by the *Wilkinson Microwave Anisotropy Probe* (WMAP) (Komatsu et al. 2009, 2010).

2 21CM SIGNATURE OF TOPHAT MINIHALOES

2.1 Spectral characteristics of top-hat minihaloes

The diffuse component of the IGM at redshift z will produce a relative differential brightness temperature against a background source of observed antenna temperature $T_B(0)$ of

$$\begin{aligned} \frac{\delta T_B(0)}{T_B(0)} &= \left[\frac{T_S}{T_B(0)(1+z)} - 1 \right] [1 - \exp(-\tau_d)] \\ &\simeq -\tau_d \left[1 - \frac{T_S}{T_B(0)(1+z)} \right] \end{aligned} \quad (1)$$

where the 21cm optical depth of the IGM with mean hydrogen density $\bar{n}_H(z)$, neutral fraction $x_{\text{HI}}(z)$, and spin temperature $T_S(z)$ is given by

$$\begin{aligned} \tau_d &= \frac{3}{32\pi} x_{\text{HI}} [1 + \delta(z)] \bar{n}_H(z) \lambda_{10}^3 \frac{A_{10}}{H(z)} \frac{T_*}{T_S(z)} \\ &\simeq 0.0046 [1 + \delta(z)] \left(\frac{x_{\text{HI}}(z)}{T_S(z)} \right) \Omega_m^{-1/2} (1+z)^{3/2} \\ &\quad \times \left[1 + \frac{1 - \Omega_m}{\Omega_m(1+z)^3} \right]^{-1/2}, \end{aligned} \quad (2)$$

with $T_B = T_B(0)(1+z)$, and where $T_* = h\nu_{10}/k_B$, $\lambda_{10} \simeq 21.1 \text{ cm}$, $\nu_{10} = c/\lambda_{10}$, k_B is the Boltzmann constant, $A_{10} \simeq 2.85 \times 10^{-15} \text{ s}^{-1}$ is the spontaneous transition rate of the 21cm hyperfine transition, and allowing for linear density fluctuations $\delta(z)$ (Field 1959a; Scott & Rees 1990; Madau et al. 1997; Meiksin 2009). The spin temperature is given by

$$T_S = \frac{T_{\text{CMB}}(z) + y_\alpha T_\alpha + y_c T_K}{1 + y_\alpha + y_c}, \quad (3)$$

(Field 1958), where $y_\alpha = (P_{10}/A_{10})(T_*/T_\alpha)$ for a de-excitation rate P_{10} of the hyperfine triplet state by $\text{Ly}\alpha$ photon scattering at the rate $P_\alpha = (27/4)P_{10}$, y_α is the colour temperature of the radiation field, $y_c = (C_{10}/A_{10})(T_*/T_K)$ for a collisional de-excitation rate C_{10} of the hyperfine triplet state, T_K is the kinetic temperature of the gas, and $T_{\text{CMB}}(z)$ is the CMB temperature at redshift z . The colour temperature relaxes rapidly to the gas kinetic temperature after 10^3 scattering times (Field 1959b; Meiksin 2006), so that $T_\alpha = T_K$ is assumed. For a $\text{Ly}\alpha$ scattering rate P_α matching the thermalization rate $P_{\text{th}} = (27/4)A_{10}T_{\text{CMB}}(z)/T_*$, the radiation field effectively couples the spin temperature to the kinetic temperature of the gas (Madau et al. 1997). The collisional de-excitation rate is computed from the rates of Allison & Dalgarno (1969) and Zygelman (2005) (taking into account the factor 4/3 difference between their definitions of the collision rate). The optical depth will typically be much smaller than unity. The signal will be either in emission or absorption against the background source, depending on the larger of T_S and $T_B(0)(1+z)$.

Superposed on any signature from the diffuse IGM in the spectrum of a background radio source will be narrow

features produced by intervening minihaloes. These again will be either in emission or absorption, depending on the brightness temperature of the source. Whilst the collapsed haloes will develop a steep internal density profile, it is useful to formulate the contribution of the minihaloes in the simplified scenario of collapsing isothermal spherical tophats. Although a simplification, it provides a straightforward fiducial model that incorporates most of the essential physics against which more sophisticated models may be compared. In particular, in the limit of negligible dissipation, it provides the expected scaling relations of the mean equivalent width on the cosmological parameters and the redshift of collapse.

The differential brightness temperature produced by intervening gas against a background source of brightness temperature $T_B(\nu)$ is given by

$$\delta T_B(\nu) = \int dl T_S(l) \frac{d\tau_\nu(l)}{dl} e^{-\tau_\nu(l)} - T_B(\nu) (1 - e^{-\tau_\nu}), \quad (4)$$

where

$$\tau_\nu(l) = \frac{3}{8\pi} A_{10} \lambda_{01}^2 \int^l dl' \frac{1}{4} x_{\text{HI}}(l') n_{\text{H}}(l') \varphi_\nu \frac{T_*}{T_S(l')} \quad (5)$$

is the optical depth from the source up to a distance l through the intervening gas of total hydrogen density $n_{\text{H}}(l)$, neutral fraction $x_{\text{HI}}(l)$ and spin temperature $T_S(l)$. The factor $1/4$ accounts for the occupation fraction of the lower hyperfine level of the hydrogen. The factor T_*/T_S accounts for stimulated emission of the 21cm line. The absorption line profile is described by $\varphi_\nu = \phi_\nu/\Delta\nu_D$, where $\phi_\nu = \pi^{-1/2} \exp\{-[\nu - \nu_{10}(1 - v(l)/c)]^2/(\Delta\nu_D)^2\}$ is the dimensionless Doppler profile with Doppler width $\Delta\nu_D = \nu_{10}b/c$ and Doppler parameter $b = (2k_{\text{B}}T/m_{\text{H}})^{1/2}$, where T is the gas temperature. The Doppler shifting of the line centre frequency by the bulk motion of the gas with flow velocity $v(l)$ along the line of sight has been included.

The observed equivalent width through an individual tophat halo at a projected comoving separation b_\perp from the centre is given by

$$w_{\nu_0}^{\text{obs}}(b_\perp) = \pm(1+z)^{-1} \int d\nu \frac{\delta T_B(\nu)}{T_B} = \pm(1+z)^{-1} \left[\frac{T_S}{T_B(z)} - 1 \right] \int d\nu (1 - e^{-\tau_\nu(b_\perp)}) \quad (6)$$

where the redshift factor converts the rest frame equivalent width to the observed frame, and the sign convention is chosen so that the equivalent width is made positive whether corresponding to emission or absorption. Here, $\tau_\nu = \tau_0 \pi^{1/2} \Delta\nu_D \varphi_\nu$. Assuming the gas is isothermal and in hydrostatic equilibrium, the line centre optical depth τ_0 for a spherical tophat collapsed at redshift z_c is given by

$$\tau_0 = \frac{3}{8\pi^{3/2}} A_{10} \lambda_{10}^3 f_c^{-2} \frac{x_{\text{HI}} \bar{n}_{\text{H}}(z_c)}{4b} \frac{2r_0}{1+z_c} \left[1 - \left(\frac{b_\perp}{f_c r_0} \right)^2 \right] \frac{T_*}{T_S}, \quad (7)$$

where the halo virialises at radius $r_v = f_c r_0/(1+z_c)$ with $f_c = (18\pi^2)^{-1/3}$. The factor f_c^{-2} accounts for the increased column density through the collapsed halo.

Typically $\tau_0 \ll 1$, in which case the observed equivalent width of a halo of mass M collapsed at redshift z_c may be expressed as

$$w_{\nu_0}^{\text{obs}}(b_\perp) = w_{\nu_0}^{\text{obs}}(0) \left[1 - \left(\frac{b_\perp}{f_c r_0} \right)^2 \right]^{1/2}, \quad (8)$$

where

$$w_{\nu_0}^{\text{obs}}(0) = \pm \frac{3}{32\pi} A_{10} \lambda_{10}^2 f_c^{-2} x_{\text{HI}} \bar{n}_{\text{H}}(0) 2r_0(M) \times \frac{(1+z_c)T_*}{T_S(z_c)} \left[\frac{T_S(z_c)}{T_B(z_c)} - 1 \right]. \quad (9)$$

It will be shown below that for either absorption against a bright radio source or for absorption or emission against the CMB, the observed equivalent width is independent of the redshift of the minihalo, depending only on its mass.

The combined absorption by the minihaloes will reduce the antenna temperature by $\exp(-\tau_l)$, so that $\delta T_B(0) = -T_B(0)(1 - e^{-\tau_l})$, where

$$\tau_l = \pm \frac{(1+z_c)^2}{\nu_{10}} \int dw_{\nu_0}^{\text{obs}} \frac{\partial^2 N}{\partial w_{\nu_0}^{\text{obs}} \partial z} w_{\nu_0}^{\text{obs}}, \quad (10)$$

where $\partial^2 N/\partial w_{\nu_0}^{\text{obs}} \partial z$ is the number of features of observed equivalent width $w_{\nu_0}^{\text{obs}}$ per unit redshift (Meiksin 2009). Values with either $\tau_l > 0$ or $\tau_l < 0$ are possible, corresponding to absorption or emission, respectively, against the radio background.

The equivalent width distribution may be computed as $\partial^2 N/\partial w_{\nu_0} \partial z = -(\partial/\partial w_{\nu_0}^{\text{obs}}) dN(> w_{\nu_0}^{\text{obs}})/dz$, where $dN(> w_{\nu_0}^{\text{obs}})/dz$ is the number of absorbers per unit redshift with observed equivalent widths exceeding $w_{\nu_0}^{\text{obs}}$. This is given by

$$\frac{dN(> w_{\nu_0}^{\text{obs}})}{dz} = (1+z) \frac{dl_p}{dz} \int dM \frac{dn}{dM} \sigma_{\text{TH}}^{\text{max}}(M) = \frac{dl_p}{dz} \int d \log M \frac{1+z}{\lambda_{\text{mfp}}(w_{\nu_0}^{\text{obs}})}, \quad (11)$$

where $dl_p/dz = (c/H(z))(1+z)^{-1}$ is the differential proper length per redshift, dn/dM is the number density of collapsed haloes of mass M per unit comoving volume, and $\sigma_{\text{TH}}^{\text{max}}(M) = \pi[b_\perp^{\text{max}}(M)]^2$ is the comoving cross-section corresponding to the maximum comoving impact parameter $b_\perp^{\text{max}}(M)$ through the halo within which the equivalent width exceeds $w_{\nu_0}^{\text{obs}}$. From Eq. (8), it is given by

$$b_\perp^{\text{max}} = f_c r_0 \left\{ 1 - \left[\frac{w_{\nu_0}^{\text{obs}}}{w_{\nu_0}^{\text{obs}}(0)} \right]^2 \right\}^{1/2}. \quad (12)$$

The last form expresses the number density per unit redshift more generally in terms of the comoving mean free path $\lambda_{\text{mfp}}(w_{\nu_0}^{\text{obs}}) = 1/(dn/d \log M) \sigma_{w_{\nu_0}^{\text{obs}}}^{\text{max}}(M)$, where $\sigma_{w_{\nu_0}^{\text{obs}}}^{\text{max}}(M)$ is the cross section through a halo of mass M giving rise to an absorption feature with observed equivalent width exceeding $w_{\nu_0}^{\text{obs}}$.

It follows from Eq. (10) that the cumulative optical depth from the ensemble of minihaloes may be expressed, after an integration by parts, as

$$\begin{aligned} \tau_l &= \frac{(1+z_c)^2}{\nu_{10}} \int dw_{\nu_0}^{\text{obs}} \frac{dN(> w_{\nu_0}^{\text{obs}})}{dz} \\ &= \frac{(1+z_c)^3}{\nu_{10}} \frac{dl_p}{dz_c} \frac{2\pi}{3} f_c^2 \int_{M_{\text{min}}}^{M_{\text{max}}} dM \frac{dn}{dM} r_0^2 w_{\nu_0}^{\text{obs}}(0) \\ &= \frac{(1+z_c)^3}{\nu_{10}} \frac{dl_p}{dz_c} \int_{M_{\text{min}}}^{M_{\text{max}}} dM \frac{dn}{dM} \Sigma_w^{\text{obs}}[f_c r_0(M)], \end{aligned} \quad (13)$$

where the last form is general, with $\Sigma_w^{\text{obs}} = \sigma_h \langle w_{\nu_0}^{\text{obs}} \rangle$ the equivalent-width weighted cross section, where $\langle w_{\nu_0}^{\text{obs}} \rangle$ is the mean observed equivalent width face-averaged over a comoving halo cross-section σ_h . More generally,

$$\Sigma_w^{\text{obs}}(b_{\perp}^{\text{max}}) = 2\pi \int_0^{b_{\perp}^{\text{max}}} db_{\perp} b_{\perp} w_{\nu_0}^{\text{obs}}(b_{\perp}). \quad (14)$$

This may be compared with the optical depth through the diffuse component of the IGM. The spin temperature will quickly couple to the CMB temperature, in which case the optical depth of the diffuse component would $\tau_d \simeq 0.011$ at $z = 10$. In the presence of either a sufficient collision rate with hydrogen atoms and electrons, or a sufficiently intense Ly α scattering rate, the spin temperature of the hydrogen will be coupled to the kinetic temperature of the gas. The resulting optical depth of the diffuse component would then increase to $\tau_d \simeq 0.13$. In the presence of heating, the optical depth would be reduced inversely with the gas temperature.

Experiments designed to measure an IGM signal against the CMB compare the signal from a neutral patch of the IGM with that towards an ionized patch, through which the CMB signal will be negligibly attenuated. For a spin temperature coupled to the gas kinetic temperature throughout the IGM, the corresponding differential brightness temperature compared with the CMB would be $T_B - T_{\text{CMB}} \simeq -330$ mK at $z = 10$. If the IGM were heated to a temperature much higher than the CMB temperature, the differential brightness temperature against the CMB, however, would convert to emission, saturating at a value of 29 mK.

The minihalo signal against the CMB may be detectable when the amount of galactic feedback is too little to decouple the spin temperature of the diffuse IGM component from that of the CMB. Since the telescope beam probing the neutral patch will encompass a large number of minihaloes, the collective optical depth of an ensemble of minihaloes determines the strength of the minihalo signal. The expression for the optical depth takes on a particularly simple form in the approximation that the systems are optically thin. If $\Upsilon(M)$ denotes the hydrogen mass fraction of a halo of total mass M , then using Eq. (9), the optical depth may be re-expressed as

$$\begin{aligned} \tau &\simeq -\frac{3}{32\pi} A_{10} \lambda_{10}^3 \frac{(1+z)^3}{H(z)} \frac{T_*}{T_{\text{CMB}}(z)} \\ &\times \frac{1}{m_{\text{H}}} \int_{M_{\text{min}}}^{M_{\text{max}}} dM \frac{dn}{dM} \Upsilon(M) M \eta_{\text{CMB}}(M), \end{aligned} \quad (15)$$

where

$$\begin{aligned} \eta_{\text{CMB}} &= x_{\text{HI}} \left[1 - \frac{T_{\text{CMB}}(z_c)}{T_S} \right] \\ &= x_{\text{HI}} \frac{\frac{P_{\alpha}}{P_{\text{th}}} \left[1 - \frac{T_{\text{CMB}}(z)}{T_K(z)} \right] + y_c \left[\frac{T_K(z)}{T_{\text{CMB}}(z)} - 1 \right]}{1 + \frac{P_{\alpha}}{P_{\text{th}}} + y_c \frac{T_K(z)}{T_{\text{CMB}}(z)}}, \end{aligned} \quad (16)$$

is the 21cm efficiency for absorption ($T_S < T_{\text{CMB}}(z_c)$) or emission ($T_S > T_{\text{CMB}}(z_c)$) against the CMB (Madau et al. 1997). The last form uses Eq. (3). Comparison with Eq. (2) shows the optical depth takes on the same form as for the diffuse IGM with $T_S(z)$ replaced by $T_{\text{CMB}}(z)$ and $\bar{n}_{\text{H}}(z)$ by $\bar{n}_{\text{H}}(z) \langle f_M \rangle$, where $\langle f_M \rangle = \bar{n}_{\text{H}}(0)^{-1} \int dM (dn/dM) \Upsilon(M) M \eta_{\text{CMB}}(M)$. The optical depth is thus proportional to the mean hydrogen mass

fraction of the IGM in haloes, weighted by the 21cm efficiency of the haloes. The resulting observed temperature differential compared with the CMB is $\delta T_B(0) \simeq -\tau T_{\text{CMB}}(0)$.

2.2 The minihalo mass function

The density distribution of minihaloes is uncertain. The resolution requirements for an N -body simulation determination are currently too prohibitive, although progress has been made from very large-scale simulations in estimating the halo number density. A minimum resolution requirement may be estimated as follows. For a simulation to represent a fair sample of the universe, the *rms* density fluctuation across it should be very small. At $z = 10$, $\sigma < 0.1$ requires a box with a comoving side exceeding $15h^{-1}$ Mpc. From Eq. (40) below, the comoving Jeans length at $z = 10$ is 7 kpc, corresponding to a Jeans mass of $M_J \simeq 5 \times 10^4 M_{\odot}$. For $h = 0.705$, these values correspond to a range of a factor of 3000 in length.

The requirements for identifying discrete haloes are similarly extreme. The simplest and most widely known estimate of the number density is based on the Press-Schechter model (Press & Schechter 1974), who derived

$$\frac{dn}{dM} = \frac{2}{\pi^{1/2}} \Omega_m \frac{\rho_{\text{crit}}(0)}{M^2} \exp(-t^2) \frac{dt}{d \log M}, \quad (17)$$

where $t = 2^{-1/2} \delta_c / \sigma(M, z)$ and including a factor of 2 fix derived by Bond et al. (1991). Here, $\sigma(M, z)$ is the *rms* fluctuation in the density field at redshift z , given by

$$\sigma^2(M, z) = \int d \log k \Delta^2(k, z) \exp(-k^2 R_f^2), \quad (18)$$

on the comoving scale R_f given by $(4\pi/3) \Omega_m \rho_{\text{crit}}(0) R_f^3 = M$, for the primordial mass fluctuation spectrum $\Delta^2(k, z)$. The factor δ_c is the density threshold a growing spherical tophat perturbation achieves in the linear growth extrapolation when the tophat collapses. Adopting the epoch of total collapse in an Einstein-deSitter universe gives $\delta_c = (3/5)(3\pi/2)^{2/3} \simeq 1.68647$. At $z = 10$, the Jeans length corresponds to $t \simeq 1$ in Eq. (17). The mass fraction of the IGM in haloes with mass above the Jeans mass is

$$\begin{aligned} f_J &= \int_{M_J}^{\infty} dM \frac{dn}{dM} \frac{M}{\Omega_m \rho_{\text{crit}}(0)} \\ &\simeq 1 - \text{erf}(1) \simeq 0.16. \end{aligned} \quad (19)$$

This would require identifying about 10^8 Jeans mass haloes in the simulation volume. For a minimum requirement of ~ 100 particles to clearly identify an individual halo (Reed et al. 2007), the simulation would need to be run with at least 10^{10} particles of mass $m_p \simeq 500 M_{\odot}$. These requirements become even more severe if better than 10% accuracy is sought, for which more than 400 particles per halo appears necessary (Bhattacharya et al. 2010). The requirements may be eased if the 21cm signature converges for halo masses above the Jeans mass, but using the results from simulations is still made problematic by numerical uncertainties such as the operational definition of a halo (Reed et al. 2007; Bhattacharya et al. 2010).

It is well-established that the Press-Schechter formula is an imperfect description of the mass function derived from N -body simulations, particularly for low mass and high mass haloes. Various modifications of the Press-Schechter

formula have been considered in the literature. One of the simplest is to allow δ_c to be a free parameter selected to match simulation results. Adopting the epoch corresponding to a collapse to the virialization radius gives instead $\delta_c = (3/5)(3/8)^{2/3}(3\pi + 2)^{2/3} \simeq 1.58272$. A choice of $\delta_c = 1.58$ was explored by Bond & Myers (1996a) in the context of galaxy clusters.

Another alternative is the estimate provided by Bardeen et al. (1986) (BBKS) based on the density of peaks in the primordial dark matter density field. The density of peaks filtered on a length scale R_f is given by

$$\frac{dn}{dM} = \frac{1}{\pi^{1/2}} \Omega_m \frac{\rho_{\text{crit}}(0)}{M^2} \exp(-t^2) G(\gamma, 2^{1/2} \gamma t) \frac{dt}{d \log M}, \quad (20)$$

where $\gamma = \sigma_1^2 / (\sigma_0 \sigma_2)$ with

$$\sigma_j^2(M, z) = \int d \log k \Delta^2(k, z) \exp(-k^2 R_f^2) k^{2j}. \quad (21)$$

and G is a function provided by Bardeen et al. (1986). The uncertainty in relating the peaks in the primordial density field to collapsed haloes that form later creates an uncertainty in the relation between the filtering scale R_f and halo mass M , with, for a gaussian density profile for example, $M = (2\pi)^{3/2} \Omega_m \rho_{\text{crit}}(0) r_s^3$, where $r_s = f_s R_f$ (Bond & Myers 1996a). More sophisticated approaches allow for the tidal forces that modify the evolution of the primordial perturbations (Bond & Myers 1996a), which can be particularly severe for small haloes in the vicinity of larger scale overdensities.

Alternatively, the results to numerical simulations may be fit by analytical approximations. Several such fitting formulas have been presented in the literature, but not down to the halo masses required. The simulations of Reed et al. (2007), however, have reached to $M \gtrsim 10^5 M_\odot$ at $z \geq 10$. The fitting formula may be expressed as

$$\frac{dn}{dM} = \frac{1}{\pi^{1/2}} \Omega_m \frac{\rho_{\text{crit}}(0)}{M^2} \exp(-t^2) H(n_{\text{eff}}, t) \frac{dt}{d \log M}, \quad (22)$$

where

$$H(n_{\text{eff}}, t) = 0.542 \left[1 + 0.901 t^{-0.6} + 0.6 G_1(t) + 0.4 G_2(t) \right] \times \exp \left[0.236 t^2 - \frac{0.0369}{(n_{\text{eff}} + 3)^2} t^{0.6} \right], \quad (23)$$

with $G_1(t) = \exp\{-[\log t - 0.576]^2 / [2(0.6)^2]\}$, $G_2(t) = \exp\{-[\log t - 0.926]^2 / [2(0.2)^2]\}$ and $n_{\text{eff}} = 6d \log t / d \log M - 3$.

Whilst it is straightforward to extrapolate Eq. (22) to lower masses, it is unclear how reliable the result would be, especially as the length scale moves more closely towards the flicker-noise limit for which $n_{\text{eff}} = -3$. The Press-Schechter and BBKS formulations may serve as useful guides. The Press-Schechter function is normalised to match Eq. (22) at $M = 3 \times 10^5 h^{-1} M_\odot$ by setting $\delta_c = 1.61$ at $z = 20$ and $\delta_c = 1.98$ at $z = 10$. As shown in Figure 1, the function somewhat exceeds the extrapolation of Eq. (22) towards $M < 3 \times 10^5 h^{-1} M_\odot$, and falls well below Eq. (22) at large masses, so that it may not serve as a reliable guide.

The BBKS approximation requires fixing f_s . This is done by matching to Eq. (22) over the mass ranges $3 \times 10^5 < M < 10^9 h^{-1} M_\odot$ at $z = 20$ and $3 \times 10^5 < M < 10^{11} h^{-1} M_\odot$ at $z = 10$. At $z = 20$, adopting $\delta_c = 1.683$ gives a slow variation of f_s over the range $3.3 > f_s > 2.4$ given

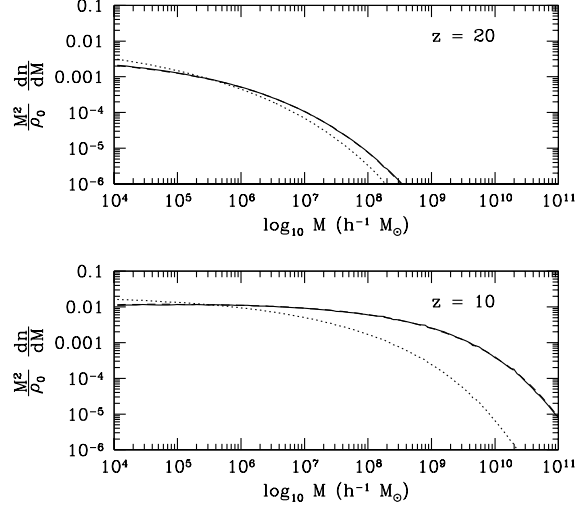


Figure 1. Dimensionless dark matter mass function ($M^2/\rho_0)dn/dM$, where $\rho_0 = \Omega_m \rho_{\text{crit}}(0)$, at $z = 20$ (top panel) and $z = 10$ (bottom panel). Shown are the fit from Reed et al. (2007) (solid lines), the BBKS approximation (dashed lines), and the Press-Schechter approximation (dotted lines). (See text.)

by $f_s \simeq 8.732 - 1.411 \log_{10} M + 0.07894(\log_{10} M)^2$. At $z = 10$, it is found that no value for f_s matches Eq. (22) for $\delta_c = 1.686$. Instead a much lower value of δ_c is required. Whilst some degeneracy exists between δ_c and f_s , a good match is obtained using $\delta_c = 1$. In this case, f_s varies slowly over the range $0.1 < f_s < 0.5$ given by $f_s \simeq 0.1303 - 0.04612 \log_{10} M + 0.007157(\log_{10} M)^2$. The fits are shown in Figure 1. The ratio of the fits to Eq. (22) is shown in Figure 2 at $z = 20$ and $z = 10$. The extrapolation of Eq. (22) to $M < 3 \times 10^5 h^{-1} M_\odot$ matches the BBKS prediction to better than 5%. This suggests either relation may be used to estimate the number of minihaloes. For the remainder of this paper, predictions are based on Eq. (22).

The ability of the BBKS density of peaks to recover Eq. (22) lends itself to an interpretation of the formation of the minihaloes within the peak-patch picture. At $z = 20$, $f_c = 1.686$ and $f_s > 1$ suggests that a minihalo forms at $z = 20$ from the merger of many peaks in the primordial density field throughout an extended patch. A similar effect was found by Bond & Myers (1996b) for the formation of clusters of galaxies at much lower redshifts. By contrast, requiring $f_c \simeq 1$ and $f_s < 1$ at $z = 10$ suggests the statistics of minihaloes is dictated by the growth of the density fluctuation over a much larger patch as it just begins to go nonlinear. The validity of these scenarios, however, would have to be assessed through the analysis of the merger histories of haloes and large-scale modulations of the density field computed by N -body simulations.

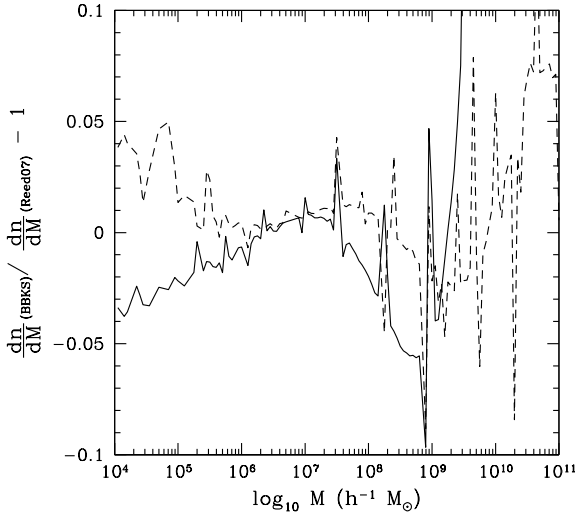


Figure 2. Deviation of the BBKS mass function from the mass function of Reed et al. (2007) at $z = 20$ (solid line) and $z = 10$ (dashed line).

2.3 21cm signature against a bright radio source

The diffuse IGM will produce an absorption signature against a bright background radio source such as a quasar or radio galaxy. For a mean neutral hydrogen density given by the cosmic mean hydrogen density, and for a hyper-fine structure coupled strongly to the CMB, so that $T_S = T_{\text{CMB}}(z)$, the optical depth of the diffuse component is $\tau_d \simeq 0.011[(1+z)/11]^{1/2}$. The absorption will appear as a step shortward of the observed wavelength of the 21cm line.

Superposed on the step will be deeper absorption features arising from overdense structures, the 21-cm forest. The equivalent width of a minihalo with line centre optical $\tau_0(b_\perp)$ a projected distance b_\perp from the cloud centre is

$$w_{\nu_0}^{\text{obs}} = (1+z)^{-1} \frac{2b}{c} \nu_{10} F[\tau_0(b_\perp)], \quad (24)$$

where $F(\tau_0)$ is a function of the line centre optical depth. For a spin temperature coupled to the post-shock temperature of the halo, using Eq.(36) below in Eq.(7) gives for the line-centre optical depth through the core ($b_\perp = 0$)

$$\tau_0(0) \simeq 0.00275(1+z_c)^{1/2} \left(\frac{M}{10^6 M_\odot} \right)^{-2/3}. \quad (25)$$

Only the lowest mass haloes at high redshift will have $\tau_0(0) > 0.1$, so that the linear curve-of-growth approximation $F(\tau_0) \simeq (\pi^{1/2}/2)\tau_0$ may generally be made.

The corresponding equivalent width may then be re-expressed as

$$w_{\nu_0}^{\text{obs}}(0) = \frac{1}{6\pi} \left(\frac{3}{2\pi^2} \right)^{1/3} A_{10} \left(\frac{\lambda_{10}}{f_c} \right)^2 \bar{n}_H(0) \times \left[\frac{3k_B T_*}{4\pi G \Omega_m \rho_{\text{crit}}(0) \bar{m}} \right]^{2/3} \left(\frac{k_B T_*}{GM \bar{m}} \right)^{1/3}$$

$$\begin{aligned} &\simeq 0.2933 \frac{\Omega_b h^2}{(\Omega_m h^2)^{2/3}} \left(\frac{M}{10^6 M_\odot} \right)^{-1/3} \text{ kHz} \\ &\simeq 0.0252 \left(\frac{M}{10^6 M_\odot} \right)^{-1/3} \text{ kHz}. \end{aligned} \quad (26)$$

It follows that the observed equivalent width is independent of the collapse redshift z_c . The strongest absorption lines arise from the lowest mass haloes because of their lower temperatures. From the dependence of r_0 and $w_{\nu_0}^{\text{obs}}(0)$ on M , and noting from Figure 1 that $M^2 dn/dM \rightarrow \text{constant}$ for low mass haloes, it follows that the absorption signal varies like $\tau_l \sim M_{\text{min}}^{-2/3}$, so that it is the lowest mass haloes M_{min} , those just sufficiently massive for shocks to form when they collapse, that dominate the overall signal.

The characteristic observed line width of the features is

$$\Delta \nu_D^{\text{obs}} \simeq 5.17(1+z_c)^{-1/2} \left(\frac{M}{10^6 M_\odot} \right)^{1/3} \text{ kHz}. \quad (27)$$

Such features would be well resolvable by an instrument with channels on the order of 1 kHz wide.

2.4 21cm signature against the CMB

In the absence of a bright background radio source, absorption or emission against the CMB signal may be detectable. In this case, the measured antenna temperature will be $T_B(0) = T_{\text{CMB}}(0) \exp(-\tau)$, where τ_l is again given by Eq. (13), where now $T_{\text{CMB}}(z) = T_{\text{CMB}}(0)(1+z)$ is used for $T_B(z)$ in Eq. (9), to give

$$w_{\nu_0}^{\text{obs}}(0) = \frac{3}{32\pi} A_{10} \lambda_{10}^2 f_c^{-2} \bar{n}_H(0) 2r_0(M) \times \frac{T_*}{T_{\text{CMB}}(0)} \eta_{\text{CMB}}. \quad (28)$$

In principle, systems in absorption against the CMB would produce a 21cm forest. From Eq. (36) for the post-shock temperature of a halo, however, it follows that requiring $T_{\text{sh}} < T_{\text{CMB}}(z_c)$ restricts the range of halo masses in absorption to $M \lesssim 7300 M_\odot$. This is smaller than the Jeans mass, so that the signal would be very weak.

Similarly, the haloes could produce discrete emission lines against the CMB. In the limit $T_S \gg T_{\text{CMB}}(z_c)$, Eq. (28) becomes

$$\begin{aligned} w_{\nu_0}^{\text{obs}}(0) &\simeq 15.07 \frac{\Omega_b h^2}{(\Omega_m h^2)^{1/3}} \left(\frac{M}{10^6 M_\odot} \right)^{1/3} \text{ kHz} \\ &\simeq 0.665 \left(\frac{M}{10^6 M_\odot} \right)^{1/3} \text{ kHz}, \end{aligned} \quad (29)$$

independent of the redshift of the halo. The detection of an individual emission line in a narrow frequency channel against a signal as weak as the CMB, however, is unlikely for the foreseeable future. More viable is the average signal from an ensemble of haloes, integrated over several channels. The observed frame equivalent width weighted comoving cross-section of the haloes is given by

$$\begin{aligned} \Sigma_w^{\text{obs}} &\simeq 135.5 \frac{\Omega_b}{\Omega_m} \left(\frac{M}{10^6 M_\odot} \right) \text{ kHz} - \text{kpc}^2 \\ &\simeq 22.6 \left(\frac{M}{10^6 M_\odot} \right)^{1/3} \text{ kHz} - \text{kpc}^2. \end{aligned} \quad (30)$$

In the limit $T_S \gg T_{\text{CMB}}(z_c)$ and using the Press-Schechter form for the halo mass function, the optical depth

Eq. (15) may be cast in the suggestive form

$$\tau_i \simeq -\frac{3}{32\pi} A_{10} \lambda_{10}^3 \frac{\bar{n}_H(z_c)}{H(z_c)} \frac{T_*}{T_{\text{CMB}}(z_c)} \times [\text{erf}(t_{\text{max}}) - \text{erf}(t_{\text{min}})], \quad (31)$$

where $\Upsilon(M) = (1 - Y)\Omega_b/\Omega_m$ was assumed. The maximum and minimum values of t , however, must be adjusted to match the halo mass function inferred from numerical simulations. The corresponding observed brightness temperature differential is

$$\delta T_B(0) \simeq (4.6\text{mK}) \Omega_m^{-1/2} (1+z_c)^{1/2} \times \left[1 + \frac{1 - \Omega_m}{\Omega_m(1+z)^3} \right]^{-1/2} f_M, \quad (32)$$

where $f_M = [\text{erf}(t_{\text{max}}) - \text{erf}(t_{\text{min}})]$ is the mass fraction of the Universe in minihaloes. The signal from minihaloes is thus a small fraction of the available signal from the IGM. At redshifts $z < 20$, when collisional decoupling from the CMB is weak within the diffuse IGM, minihaloes may dominate the signal until Lyman resonance line radiation becomes available to sufficiently decouple the spin state of the hydrogen atoms in the diffuse IGM from the CMB. The signal from the diffuse IGM, however, will dominate over that of the minihaloes once the mass-averaged 21cm efficiency of the diffuse component exceeds the mass fraction of the Universe in minihaloes.

3 THE DYNAMICAL MINIHALO MODEL

3.1 Model parameterization

Spherical minihalo models for intergalactic gas clouds with the gas confined by dark matter haloes were introduced by Ikeuchi (1986); Rees (1986), with the lower mass end limited by that required to bind photoionised gas. Recognizing that cosmological haloes are in general dynamical, with the gas either collapsing or expanding, Bond et al. (1988) extended the models by building the haloes from growing spherical cosmological density perturbations. Since the haloes form from the merger of smaller haloes, there is some freedom in the choice of the initial linear gas density profile. Whilst a tophat perturbation is simplest, Bond et al. (1988) chose a gaussian profile as it was found to best represent the final virialised halo density profile. In this paper, a tophat initial density profile is adopted for its simplicity, since the gas density will respond to the gravitational potential of the dark matter and gas combined, which is not very sensitive to the underlying density profile of the dark matter.

The temperature and residual ionisation of the background unperturbed IGM are solved for using RECFast (Seager et al. 2000). The temperature (in K) is fit to better than 10% accuracy by

$$\begin{aligned} T_K &= 0.023(1+z)^{1.95} && ; 6 < z \leq 60 \\ &= 0.146(1+z)^{1.50} && ; 60 < z \leq 300 \\ &= 1.46(1+z)^{1.10} && ; 300 < z \leq 500 \\ &= T_{\text{CMB}} && ; z > 500. \end{aligned} \quad (33)$$

The residual ionisation fraction $n_e/n_{\text{H,Tot}}$ is fit to better

than 5% by

$$\begin{aligned} \frac{n_e}{n_{\text{H,Tot}}} \times 10^4 &= 1.8 + 0.00176(1+z)^{1.5} && ; 6 < z \leq 30 \\ &= 2.0 + 0.00082(1+z)^{1.40} && ; 30 < z \leq 100 \\ &= 2.0 + 0.00366(1+z)^{1.1} && ; 100 < z \leq 300 \\ &= 0.0124(1+z) && ; 300 < z. \end{aligned} \quad (34)$$

As galaxies or active nuclei form in the Universe, the radiation from these systems may heat the IGM temperature to higher values. The hydrodynamical models are run without this heat input to provide a reference point for minimal heating. The effect of a warm diffuse IGM on the 21cm signatures, however, is also explored.

The spherical collapse model forms a two parameter family of solutions for a growing spherical perturbation. A convenient choice for the parameters is the total halo mass and epoch of collapse. For the tophat collapse of a halo of mass M and comoving radius r_0 , with $M = (4/3)\pi\rho_M(z)[r_0/(1+z)]^3$ where $\rho_M(z)$ is the total mass density at high redshifts z when vacuum energy contributes negligibly, the infall velocity v_{in} is given by

$$\frac{1}{2}v_{\text{in}}^2 = \frac{GM}{r_v} = 2 \left(\frac{3\pi}{2} \right)^{2/3} \frac{GM}{r_0} (1+z_c), \quad (35)$$

where z_c is the collapse redshift (Meiksin 2009). The corresponding post-shock gas temperature in the strong shock limit, taking the shock velocity to be v_{in} , is given by (for a monatomic gas) $T_{\text{sh}} = (3/4)^2 T_{\text{virial}}$, where $(3/2)k_B T_{\text{virial}} = GM\bar{m}/r_v$, or

$$\begin{aligned} T_{\text{sh}} &= \frac{9}{8} \left(\frac{2\pi^2}{3} \right)^{1/3} (1+z_c) \frac{GM\bar{m}}{k_B r_0} \\ &\simeq 1330(1+z_c) \frac{M/(10^6 M_\odot)}{r_0/\text{kpc}} \text{K} \\ &\simeq 72.1(1+z_c) \left(\frac{M}{10^6 M_\odot} \right)^{2/3} \text{K}, \end{aligned} \quad (36)$$

where \bar{m} is the mean mass per particle, assumed to be neutral primordial hydrogen and helium. This is slightly below the nominal mean ‘‘binding temperature’’ of the gas, defined by $(3/2)k_B T_{\text{bind}}/\bar{m} = E_{\text{bind}}/M_b \simeq (3/5)GM/r_v$ for a baryonic mass in the halo of M_b , and approximating the halo as having uniform density. The temperature may be expressed as

$$\begin{aligned} T_{\text{bind}} &= \frac{2}{5} \frac{GM\bar{m}}{k_B r_v} = \frac{16}{15} T_{\text{sh}} \\ &\simeq 76.9(1+z_c) \left(\frac{M}{10^6 M_\odot} \right)^{2/3} \text{K}. \end{aligned} \quad (37)$$

These temperatures may be compared with the temperature resulting from the adiabatic compression of the gas in the collapsed halo. For an increase in the gas density by the factor $\rho_h/\rho_M = f_c^{-3} = 18\pi^2$, the temperature will increase by the factor $T_{\text{ad}}/T_K = (\rho_h/\rho_M)^{2/3} = f_c^{-2}$. Using Eq. (33), the resulting adiabatic compression temperature for $6 < z_c < 60$ is

$$T_{\text{ad}} \simeq 0.73(1+z_c)^{1.95} \text{K}. \quad (38)$$

When this temperature exceeds T_{sh} , the gas in the collapsed halo will contract adiabatically rather than shock. This will

occur for halo masses smaller than a minimal halo shock mass

$$M_{\text{sh}} \simeq 1020(1+z_c)^{1.425} M_{\odot}. \quad (39)$$

If the IGM is heated, M_{sh} will increase. For example, scaling the unperturbed IGM temperature by the CMB temperature according to $fT_{\text{CMB}}(z)$ results in the minimum shock mass $M_{\text{sh}} \simeq 1.3 \times 10^6 f^{3/2} M_{\odot}$, independent of redshift.

At the low mass end, the baryonic fluctuations are restricted by thermal pressure support, providing a lower limit to the minihaloes which contribute to the 21cm signal before the fluctuations dissolve into sound waves. It is shown below that the high mass end is limited by the onset of star formation.

The approach of Bond et al. (1988) is used to describe the collapse of spherical mass shells, with the equations of hydrodynamics solved for numerically. In this paper, the numerical methods of Meiksin (1994) are used. The gas temperature is solved for including atomic collisional and radiative processes, as described in Meiksin (1994), and cooling by molecular hydrogen. The ionization state of the gas is computed as well in order to account for hydrogen recombinations within the halo cores. The computation of molecular hydrogen formation and cooling is described in the Appendix.

3.2 Lower limiting mass

The fluctuations in the baryonic component are filtered at short length scales by the homogenising effect of sound waves on scales comparable to the Jeans length. For linear perturbations, the Jeans length is $\lambda_J = c_s(\pi/G\rho_M)^{1/2}$, where c_s is the sound speed in the gas and ρ_M is the total mass density (Peebles 1980). Using the kinetic temperature from Eq. (33), this corresponds to a proper Jeans length and total halo mass $M_J = (4\pi/3)\rho_M(z)\lambda_J^3$ for adiabatic fluctuations at redshift z of

$$\lambda_J \simeq 2.2(1+z)^{-0.525} \text{ kpc}; \quad M_J \simeq 1800(1+z)^{1.425} M_{\odot}, \quad (40)$$

for $6 < z \leq 60$.

The Jeans mass is only an approximation to the lower limiting mass. Lower mass haloes will still contribute a non-negligible 21cm absorption signal against a bright background radio source distinguishable from the diffuse IGM. As discussed in Sec. 2.3 above, the cumulative absorption signal is dominated by the lowest mass haloes still able to retain their gas.

Haloes with mass below the Jeans mass will also contribute an emission signal against the CMB provided $T_{\text{sh}} > T_{\text{CMB}}$, or $M > 7300 M_{\odot}$, although with a reduced 21cm efficiency. An illustrative computation of a $2.0 \times 10^4 M_{\odot}$ halo is shown in Figure 3 at $z = 20$. Despite the halo's being well below the Jeans mass $M_J \simeq 1.4 \times 10^5 M_{\odot}$ at $z = 20$, its 21cm efficiency is appreciable within the core. In fact, the halo mass is below the critical mass required for a shock to form, as given by Eq. (39). The gas temperature is determined instead by the adiabatic flow of the gas as it falls into the halo and establishes hydrostatic equilibrium, settling at the binding temperature, Eq. (37), within the core. The mass-weighted efficiency over the virial radius is $\langle \eta_{\text{CMB}} \rangle \simeq 0.15$. Because of the large number of such small haloes, their net

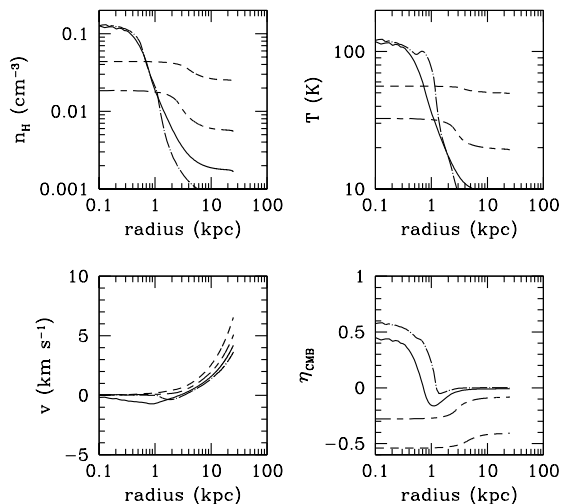


Figure 3. Evolution of the fluid variables for a $2 \times 10^4 M_{\odot}$ top hat spherical perturbation collapsing at $z_c = 20$. The Jeans mass at this epoch is $M_J \simeq 1.4 \times 10^5 M_{\odot}$. Shown are the hydrogen density (top left panel), gas temperature (top right panel), fluid velocity (bottom left panel) and 21cm efficiency η_{CMB} (bottom right panel), all as functions of comoving radius. The curves correspond to $z = 50$ (dashed line), $z = 30$ (short-dashed long-dashed line), $z = 20$ (solid line) and $z = 15$ (dotted-dashed line). The peak temperature at $z = 20$ matches the predicted binding temperature $T_{\text{bind}} \simeq 119$ K (see text).

contribution to the 21cm signatures is non-negligible, particularly at high redshifts.

3.3 Upper limiting mass

It has long been suggested that the first collapsing Jeans unstable gaseous structures in a Big Bang cosmology would have masses on the order of $10^5 - 10^6 M_{\odot}$ (Gamow 1948; Peebles & Dicke 1968), with star formation triggered by molecular hydrogen cooling following the formation of H_2 through gas phase processes with H^- and H_2^+ acting as catalysts (Saslaw & Zipoy 1967; Peebles & Dicke 1968; Hirasawa 1969). This picture has survived remarkably well in contemporary cosmological models dominated by cold dark matter, with comparably small masses for the first collapsing objects inferred (Bond & Szalay 1983; Blumenthal et al. 1984; Peebles 1984; Blumenthal et al. 1985; Ostriker & Gnedin 1996; Abel et al. 2000; Fuller & Couchman 2000; Machacek et al. 2001; Reed et al. 2005).

A major outstanding uncertainty is how the first generation of stars affects subsequent star formation. Early models suggested Lyman-Werner photons from the first stars will dissociate molecular hydrogen in the surrounding gas and inhibit star formation in haloes with temperatures below 10^4 K, when atomic cooling dominates (Haiman et al. 1997a,b). Subsequent analyses have shown the picture is much more complicated. Self-shielding will

limit the radiative transport of the Lyman-Werner photons. Whilst hot stars will photoionise their surroundings, partial ionisation may enhance the rate of molecular hydrogen formation, as would sources of x-rays, negating the dissociating effects of the UV radiation from early sources (Haiman et al. 2000). Within relic H II regions, molecular hydrogen reforms as the gas recombines, re-enabling star formation. The injection of dust would provide still an additional mechanism for molecular hydrogen formation. The injection of metals from supernovae would accelerate cooling. The feedback from star formation on subsequent generations of stars has been considered widely in the literature, eg. (Couchman & Rees 1986; Mac Low & Shull 1986; Dekel & Rees 1987; Ostriker & Gnedin 1996; Haiman et al. 1997a; Omukai & Nishi 1999; Glover & Brand 2001; Machacek et al. 2001; O’Shea et al. 2005; Yoshida et al. 2007; Wise & Abel 2007; Whalen et al. 2008; Mesinger et al. 2009; Whalen et al. 2010; Gnedin 2010). To allow for the possibility that the first generation of stars completely inhibits subsequent molecular hydrogen formation, a set of models with no molecular hydrogen formation is also computed.

To account for star formation, the creation of molecular hydrogen through gas phase reactions is computed during the collapse. Only formation via H^- is included, as the added molecular hydrogen formed via H_2^+ is negligible (Palla et al. 1983; Lepp & Shull 1984). When the cooling time is shorter than the characteristic inflow time, the gas will be thermally unstable (Malagoli et al. 1987; Balbus & Soker 1989). Overdense pockets of gas are then assumed to cool rapidly and are removed from the flow isochorically (Meiksin 1988). When the cooling time is shorter than the inflow time, mass is removed from the flow and converted into stars at the rate

$$\dot{\rho}_* = q_* \rho / t_{\text{cool}}, \quad (41)$$

where t_{cool} is the net cooling rate within a gas shell, and q_* is a dimensionless efficiency coefficient of order unity.

Once an adequate mass of stars accumulates within a halo, it is presumed that a sufficient number of massive stars will have formed to photoionise the cloud or drive a wind through it via the mechanical energy input from wind losses and supernovae and completely disperse the gas in the cloud. For a Salpeter stellar initial mass function with a minimum stellar mass of $1M_\odot$ and maximum mass of $100M_\odot$, an instantaneous burst with a total stellar mass of 10^3M_\odot formed will produce an ionizing luminosity of $10^{49.8} \text{ ph s}^{-1}$ for a duration of $3.5 \times 10^6 \text{ yr}$, assuming a metallicity of 0.05 solar (Leitherer et al. 1999). Sufficient photons would be produced to photoionize $6 \times 10^6 M_\odot$ of hydrogen, and likely lead to the photo-evaporation of the gas in the halo.

Even if radiative recombinations radiated away almost all the photoionization energy, typically at least one star as massive as $50M_\odot$ will also be produced, corresponding to a massive O-star. Such a star has a lifetime of under 10^6 yr , after which it will explode as a Type II supernova with a characteristic mechanical energy input of 10^{51} erg . Spreading the energy over a characteristic halo baryon mass of $10^5 M_\odot$ corresponds to a gas temperature of $T_{\text{SN}} \simeq 7 \times 10^4 \text{ K}$. Even allowing for 90% of the energy to radiate away, this is more than adequate to unbind the gas. A threshold of $10^3 M_\odot$ is therefore used as a criterion for sufficient star formation to disperse the gaseous content of the halo. It is

found that this quantity of stars forms soon after the halo collapses. It is also found that the epoch and minimal halo mass for forming sufficient stars to disrupt the halo is not very sensitive to the assumed parameters, such as the star formation efficiency q_* or the minimum required threshold of stars formed.

More generally, an upper limit to the halo mass below which star formation will disrupt a halo may be estimated as follows. After 10^7 yrs , the formation of $M_* = 10^3 M_\odot$ of stars with masses between $1 - 100 M_\odot$ will produce approximately 10^{52} erg of mechanical energy in the form of winds and supernovae ejecta (ranging from $10^{51.7} - 10^{51.9} \text{ erg}$ for 0.05 solar to solar metal abundances) (Leitherer et al. 1999). Allowing for a fraction f_{heat} of this energy to go into heating the gas, and for a fraction f_b of baryons for a total halo mass M , setting $(3/2)k_B T_{\text{heat}} / \bar{m} = (f_{\text{heat}} / f_b)(E_3 / M)(M_* / 1000 M_\odot)$, where E_3 is the mechanical energy input from the formation of $10^3 M_\odot$ of stars, gives a characteristic gas temperature to which the baryons will be heated of

$$T_{\text{heat}} \simeq 2.95 \times 10^5 f_{\text{heat}} E_{3,52} M_{*,3} M_6^{-1} \left(\frac{f_b}{0.167} \right)^{-1} \text{ K}, \quad (42)$$

where $E_{3,52} = E_3 / 10^{52} \text{ erg}$, $M_{*,3} = M_* / 10^3 M_\odot$ and $M_6 = M / 10^6 M_\odot$. Comparison with the binding temperature from Eq. (37) gives for the minimum halo mass required to retain the baryons ($T_{\text{heat}} < T_{\text{bind}}$),

$$M_{6,\text{min}} = 137 f_{\text{heat}}^{3/5} \left(\frac{f_b}{0.167} \right)^{-3/5} E_{3,52}^{3/5} M_{*,3}^{3/5} (1 + z_c)^{-3/5}. \quad (43)$$

For $f_{\text{heat}} = 0.5$, at $z_c = 20$ this requires a minimum halo mass of $M > 1.5 \times 10^7 M_\odot$, corresponding to a post-shock temperature of $T_{\text{sh}} \simeq 9200 \text{ K}$ from Eq. (36). This mass is well above the halo masses found below required to form $10^3 M_\odot$ of stars.

Previous estimates of the 21cm signature have not included the role played by molecular hydrogen cooling, presuming that molecular hydrogen is dissociated by a metagalactic UV radiation field produced by early stars, so that star formation becomes dominated only by more massive ($10^7 - 10^8 M_\odot$) haloes (Haiman et al. 1997a). Since it is the lower mass haloes that form first, and the gas within them does not survive long once the first stars form within them, it is unclear whether a sufficiently strong radiation field will develop at early epochs. Nonetheless, both models with and without molecular hydrogen formation are considered.

An illustrative computation including molecular hydrogen formation is presented in Figure 4 for a $1.3 \times 10^6 M_\odot$ halo collapsing at $z = 20$. The corresponding post-shock temperature is 1770 K from Eq. (36), well below the temperature required for collisional ionisation. The central temperature in the halo lies below this value because of efficient molecular hydrogen cooling. A comparison run with molecular hydrogen cooling turned off gives a central temperature of $T \simeq 2040 \text{ K}$. The evolution of the H_2 fraction for the run is shown in Figure 5, along with the stars formed following H_2 cooling. The column density is computed along lines of sight through a sphere defined by the turn-around radius at each epoch, except at $z = 50$, for which the comoving radius of the initial perturbation is used. It is found that by $z = 20.05$, shortly before the collapse epoch, $10^3 M_\odot$ of stars has formed for $q_* = 1$.

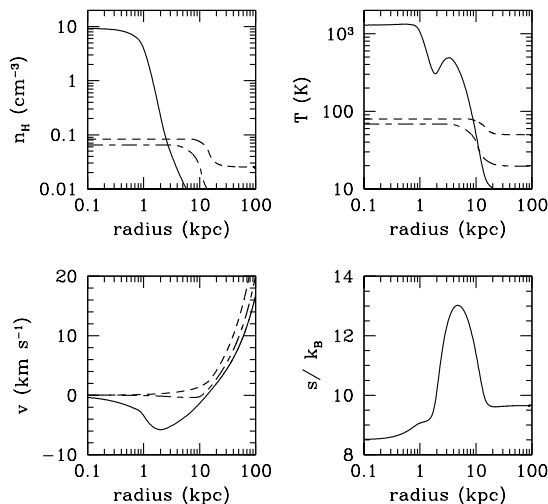


Figure 4. Evolution of the fluid variables for a $1.3 \times 10^6 M_\odot$ top hat spherical perturbation collapsing at $z_c = 20$. Shown are the hydrogen density (top left panel), gas temperature (top right panel), fluid velocity (bottom left panel) and entropy per particle (in units of k_B) (bottom right panel), all as functions of comoving radius. The curves correspond to $z = 50$ (dashed line), $z = 30$ (short-dashed long-dashed line), and $z = 20.05$ (solid line), by which $10^3 M_\odot$ of stars has formed. The peak temperature at $z = 20.05$ lies somewhat below the predicted post-shock temperature of $T_{\text{sh}} \simeq 1770$ K because of efficient molecular hydrogen cooling.

The entropy generation by the shock just within the turnaround radius results in an inverted entropy profile, as shown in Figure 4. (The entropy per particle is computed as $s = k_B \log(T^{3/2}/n_H)$.) The inflowing gas may become convectively unstable and the gas turbulent within the core, although the timescale $t_{\text{BV}} = [(2/3)(g/k_B)|ds/dr|]^{-1/2}$ (the Brunt-Väisälä timescale), where g is the gravitational acceleration, is long at these radii. At $z = 20.05$, it is shortest at $r \lesssim 10$ kpc (comoving), where $t_{\text{BV}} \simeq 69$ Myr. After this time, a spherically-symmetric computation will no longer be able to follow the evolution of the system in detail. Because the mechanical energy input by the most massive stars formed will eject the gas on a shorter timescale, however, the halo will be evacuated before becoming convective. Haloes that reach rapid cooling prior to their collapse redshifts will contribute negligibly to the 21cm signature by the time the dark matter collapses. This forms a natural upper limit to the mass range of the haloes that do contribute.

The central temperatures found for the collapsing haloes are shown in Figure 6 for a range of halo masses and redshifts. At low masses, the values with and without molecular hydrogen cooling both agree well with the expected post-shock temperature, as given by Eq. (36). Whilst the temperature without molecular hydrogen cooling continues to agree well with the expected post-shock temperature at higher masses, the temperature reaches a ceiling of $T \lesssim 1400$ K when molecular hydrogen cooling is included.

In the case with molecular hydrogen formation suppressed, for halo masses increasingly higher than $10^6 M_\odot$,

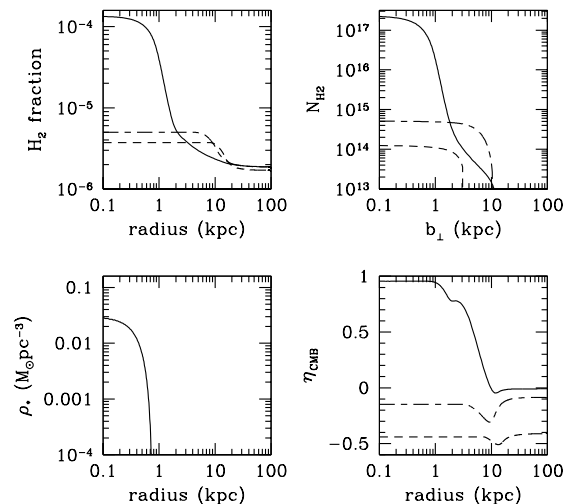


Figure 5. Evolution of the H_2 fraction (top left panel) and density of stars formed (bottom left panel) for a $1.3 \times 10^6 M_\odot$ top hat spherical perturbation collapsing at $z_c = 20$, as a function of comoving radius. The curves correspond to $z = 50$ (dashed line), $z = 30$ (short-dashed long-dashed line), and $z = 20.05$ (solid line), by which $10^3 M_\odot$ of stars has formed. The mass-weighted mean 21cm emission efficiency within the virial radius is $\langle \eta_{\text{CMB}} \rangle \simeq 0.90$ at the final time. During its growing phase, the perturbation would appear in absorption against the CMB (bottom right panel).

the central temperature reaches values increasingly higher than the predicted post-shock temperature of Eq. (36). The higher temperatures arise from double compression phases as the dark matter halo collapses and virialises. This is illustrated in Figure 7 for a $6.8 \times 10^6 M_\odot$ halo. By $z = 20.6$, the dark matter halo has substantially collapsed, and the gas shock heats to a temperature of $T > 1000$ K. As gas continues to flow inwards, the accreted hydrogen mass within the core approaches the dark matter mass and the gaseous core becomes increasingly self-gravitating. The gas flowing onto the gas core enters a transient strongly supersonic phase of near free fall velocity, as the pressure has not yet had time to establish hydrostatic balance. During this phase, the infalling gas adiabatically expands, resulting in a dip in the temperature, before coming to rest onto the core, where it compresses and converts its kinetic energy into additional heat. The result is a core with a central temperature exceeding T_{sh} and approaching T_{virial} . The gas within the halo is not isothermal, although an isothermal shell dominates the outer portions. Most of the mass, however, is in the core, where the central hydrogen exceeds the cosmological mean density by a factor well in excess of f_c^{-3} by $z = 20.1$.

The trend of an increasing central temperature compared with the post-shock temperature with increasing halo masses is apparent in Figure 6. For central temperatures $T \lesssim 8500$ K, atomic cooling through the collisional excitation of $\text{Ly}\alpha$ becomes efficient, and stars are presumed to form according to Eq. (41), as for the case with molecular hydrogen cooling. The breaking of the scaling relation

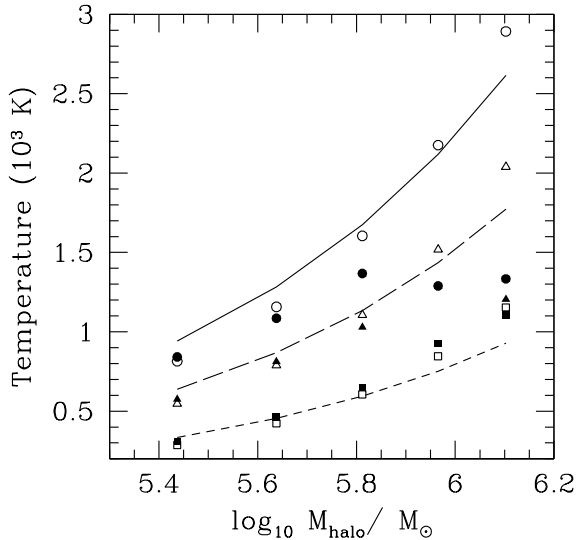


Figure 6. Central temperature as a function of halo mass. Results from numerical computation are shown at $z = 10$ (squares), 20 (triangles) and 30 (circles). Results including H_2 cooling are shown as solid symbols; open symbols show results without H_2 cooling. The curves show the expected post-shock temperature from Eq. (36), at $z = 10$ (short-dashed line), 20 (long-dashed line) and 30 (solid line). Molecular hydrogen cooling restricts the core temperature to $T < 1400$ K. With molecular hydrogen formation suppressed, the central temperature of increasingly more massive haloes approaches the virial temperature.

with mass predicted by Eq. (36) results in a departure from cosmological self-similar accretion expected in an Einstein-deSitter universe (Fillmore & Goldreich 1984; Bertschinger 1985). The reasons for the departure are examined in § 5.5.

In the presence of molecular hydrogen cooling, the maximum halo mass for which fewer than $10^3 M_\odot$ of stars form prior to the collapse of the halo is fit to 10% accuracy over $8 < z_c < 30$ by

$$M_{1000} \simeq 10^6 \left(\frac{26}{1+z_c} \right)^{1/2} M_\odot. \quad (44)$$

This agrees well with fully three-dimensional hydrodynamical simulations of the minimum halo mass of typically $10^5 - 10^6 M_\odot$ required for star formation at high redshifts (Abel et al. 2000; Fuller & Couchman 2000; Machacek et al. 2001).

If molecular hydrogen formation is suppressed, higher mass haloes in which $\text{Ly}\alpha$ cooling becomes efficient are required for stars to form. In the absence of molecular hydrogen formation, the maximum halo mass for which fewer than $10^3 M_\odot$ of stars form prior to the collapse of the halo is fit to 10% accuracy over $8 < z_c < 50$ by

$$M_{1000}^{\text{noH}_2} \simeq 9.1 \times 10^6 \exp[-(1+z_c)/51] M_\odot. \quad (45)$$

These masses are about a factor 5 greater than found when molecular hydrogen cooling is included.

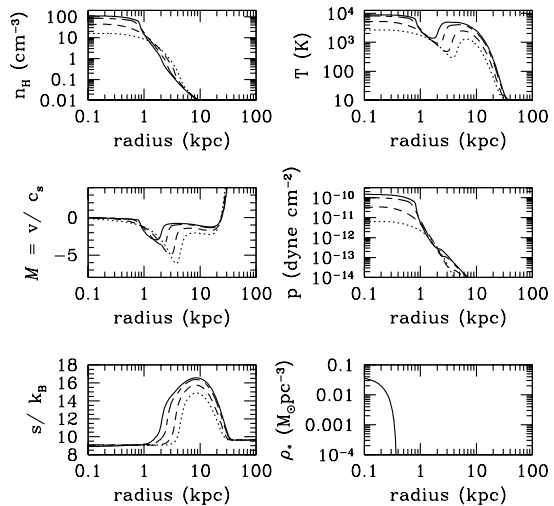


Figure 7. Evolution of the fluid variables for a $6.8 \times 10^6 M_\odot$ top-hat spherical perturbation leading up to the collapse epoch of $z_c = 20$, with H_2 cooling suppressed. Shown are the hydrogen density (top left panel), gas temperature (top right panel), fluid velocity expressed as a Mach number (middle left panel), gas pressure (middle right panel), entropy per particle (in units of k_B) (bottom left panel) and density of stars formed (bottom right panel), all as functions of comoving radius. The curves correspond to $z = 20.6$ (dotted line), $z = 20.4$ (dashed line), $z = 20.2$ (short-dashed long-dashed line), and $z = 20.1$ (solid line), soon after which $10^3 M_\odot$ of stars has formed. The peak temperature at $z = 20.1$ lies above the predicted post-shock temperature of $T_{\text{sh}} \simeq 5430$ K, approaching instead the virial temperature $T_{\text{virial}} \simeq 9660$ K, resulting in efficient atomic hydrogen cooling and star formation.

3.4 21cm signature against a bright radio source

The absorption against a bright background source is computed from Eq. (4). An illustration is given in Figure 8 for a halo with mass $M = 0.9 \times 10^6 M_\odot$, including H_2 cooling. (The results for the case with H_2 cooling suppressed are nearly identical for this mass.) The absorption features are found not to evolve rapidly for a given halo mass, showing only a mild increase in the line-centre optical depth with time. The increase results from the continual inflow of material and the departure from self-similar accretion, as discussed below. The trend of increasing optical depth with decreasing collapse epoch is contrary to the redshift scaling expectation for an idealised tophat halo, Eq. (25), which predicts a decreasing optical depth. The inflow also produces a substantially broader and shallower feature than occurs when the velocity broadening is suppressed.

The profiles shown in Figure 8 were generated by integrating only along distances within the virial radius of the minihalo. An observed feature would include the absorption by the IGM in the surrounding gas. In Figure 9, profiles are shown at several impact parameters integrating out to the diffuse IGM. The intergalactic diffuse component is clearly visible in the wings of the features beyond a frequency offset of 4 kHz (in the observed frame). Since individual features

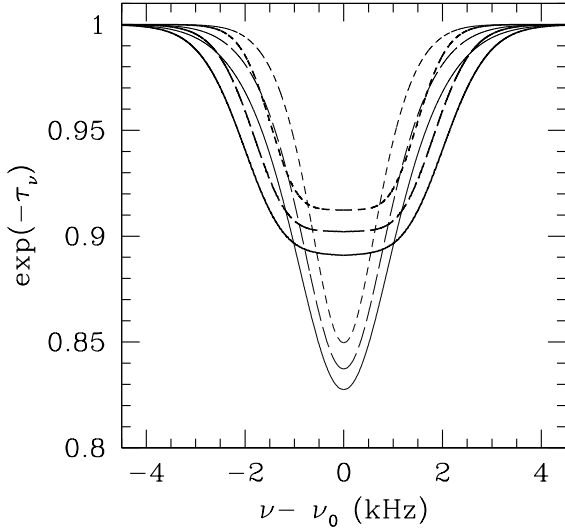


Figure 8. Evolution of the absorption feature against a bright background source along a line of sight through the centre of a halo of mass $M = 0.9 \times 10^6 M_\odot$, for collapse epochs of $z_c = 15$ (short-dashed line), 10 (long-dashed line), and 8 (solid line). Profiles are shown both including the broadening from the line-of-sight peculiar velocities (heavy lines), and without the peculiar velocity contribution (light lines). The frequency offset from line centre is in the observed frame.

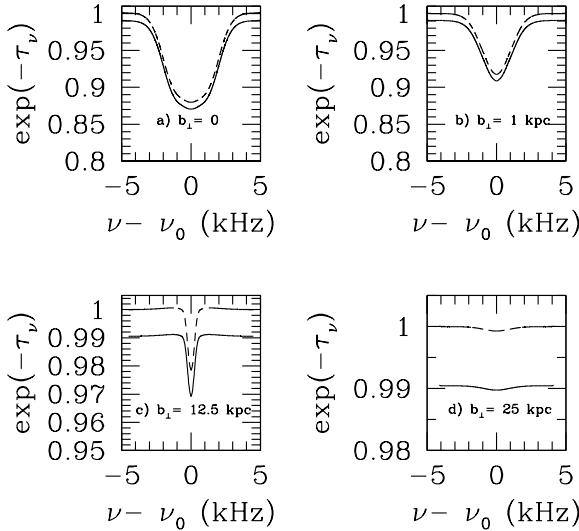


Figure 9. Optical depth as a function of observed 21cm frequency for a halo of mass $M = 0.9 \times 10^6 M_\odot$ and collapse epoch of $z_c = 8$. Results shown for lines of sight at a) $b_\perp = 0$, b) $b_\perp = 1$ kpc (co-moving), c) $b_\perp = r_{t.a.}$ and d) $b_\perp = 2r_{t.a.}$, where $r_{t.a.}$ is the turnaround radius of the halo. The optical depth is computed through a sphere extending to the linear regime of the perturbation. Shown are the signal through the sphere (solid lines), and after subtracting off the values at 4 kHz (dashed lines).

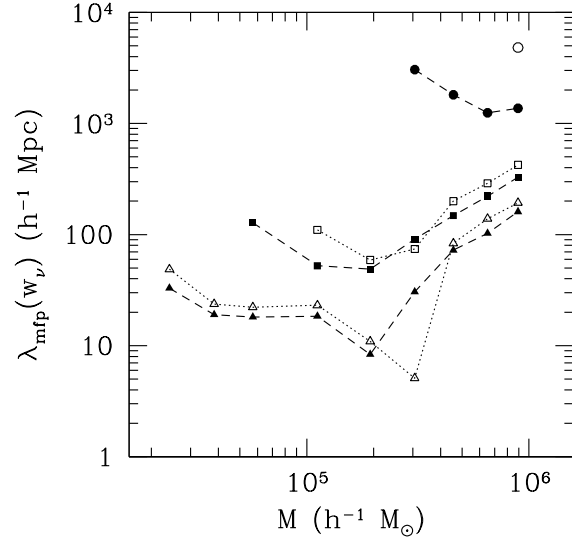


Figure 10. Comoving mean free path for haloes collapsing at $z_c = 8$ (solid symbols) and $z_c = 10$ (open symbols) for cross sections giving rise to absorption features against a bright background source with observed equivalent widths $w_{\nu_0}^{\text{obs}} > 0.1$ kHz (triangles), $w_{\nu_0}^{\text{obs}} > 0.2$ kHz (squares) and $w_{\nu_0}^{\text{obs}} > 0.4$ kHz (circles).

would be measured relative to the diffuse absorption level, the offset at 4 kHz serves as a useful operational definition for the baseline relative to which the equivalent width of the feature would be determined. This definition for the absorption equivalent width against a bright background source will be used throughout the remainder of this paper.

According to Eq. (11), the contribution of a halo of mass M to absorption features with an observed equivalent width exceeding a given $w_{\nu_0}^{\text{obs}}$ scales inversely with the mean free path $\lambda_{\text{mfp}}(w_{\nu_0}^{\text{obs}})$ for intercepting a halo along a line of sight with observed equivalent width exceeding $w_{\nu_0}^{\text{obs}}$. The mean free paths are shown for haloes with H_2 cooling collapsing at $z_c = 8$ in Figure 10 for equivalent width limits $w_{\nu_0}^{\text{obs}} > 0.1$, 0.2 and 0.4 kHz. Most of the systems with $w_{\nu_0}^{\text{obs}} > 0.1$ arise from haloes in the mass range $4 \times 10^4 - 3 \times 10^5 h^{-1} M_\odot$.

3.5 21cm signature against the CMB

The collapsing haloes will produce emission features relative to the CMB. The observed temperature differentials are shown in Figure 11 for a halo with mass $M = 0.9 \times 10^6 M_\odot$, including H_2 cooling. (The case with H_2 cooling suppressed differs little for this mass.) The increase in the brightness temperature for later collapse epochs arises from the continual inflow of material. As in the case for absorption against a bright background source, the infall broadens the feature and reduces its amplitude compared with the result when the velocity contribution is suppressed.

Emission against the CMB is not very sensitive to the signature from the infalling gas surrounding the minihalo. This is because collisions are able to decouple the hydrogen spin structure from the CMB only at sufficiently large

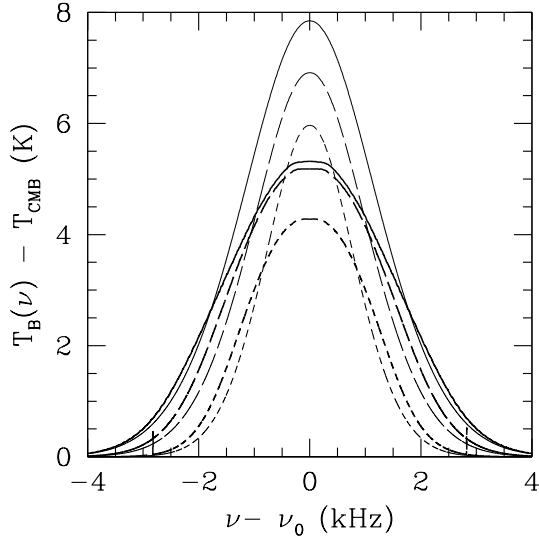


Figure 11. Evolution of the observed brightness temperature relative to the CMB along the line of sight through the centre of a halo of mass $M = 0.9 \times 10^6 M_\odot$, for collapse epochs of $z_c = 15$ (short-dashed line), 10 (long-dashed line), and 8 (solid line). Profiles are shown both including the broadening from the line-of-sight peculiar velocities (heavy lines), and without the peculiar velocity contribution (light lines). The frequency offset from line centre is in the observed frame.

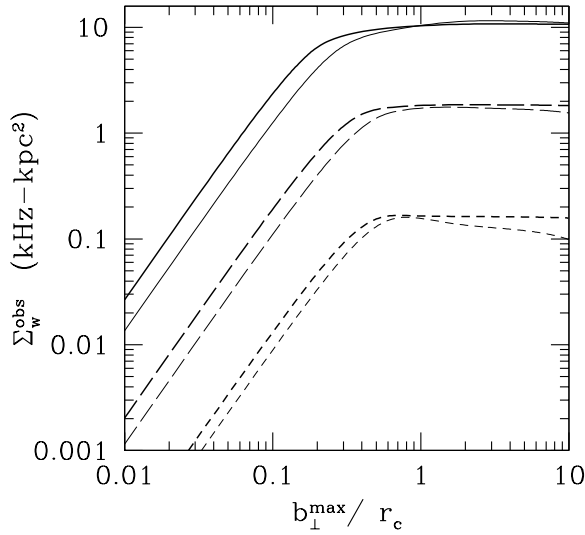


Figure 12. Observed integrated equivalent width weighted comoving cross section for emission against the CMB as a function of comoving maximum impact parameter b_\perp^{\max} , normalized by the core radius. Shown for haloes of mass $M = 0.9 \times 10^6 M_\odot$ (solid lines), $M = 0.3 \times 10^6 M_\odot$ (long-dashed lines), and $M = 0.8 \times 10^5 M_\odot$ (short-dashed lines), for collapse epochs of $z_c = 8$ (heavy lines) and 15 (light lines). The turnaround radius corresponds to $b_\perp^{\max}/r_c \simeq 3.89$.

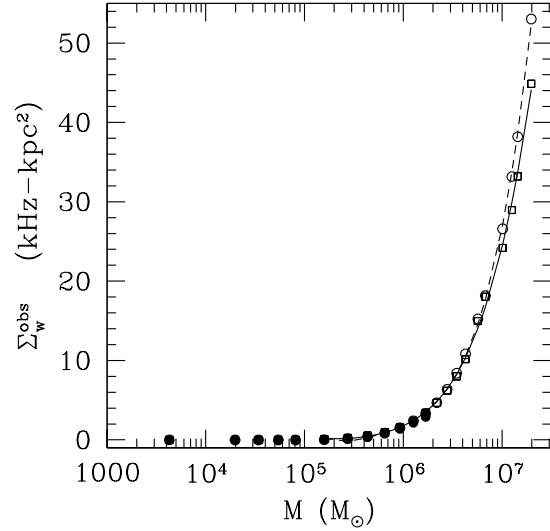


Figure 13. Comoving equivalent width weighted cross section (in kHz-kpc^2) for emission against the CMB, as a function of halo mass for haloes collapsing at $z_c = 10$ (squares) and $z_c = 20$ (circles). The cross section is shown in the observed frame. Shown for models including H_2 cooling (solid symbols) and without (open symbols). Also shown are fits for models without H_2 cooling at $z_c = 10$ (solid line) and $z_c = 20$ (dashed line).

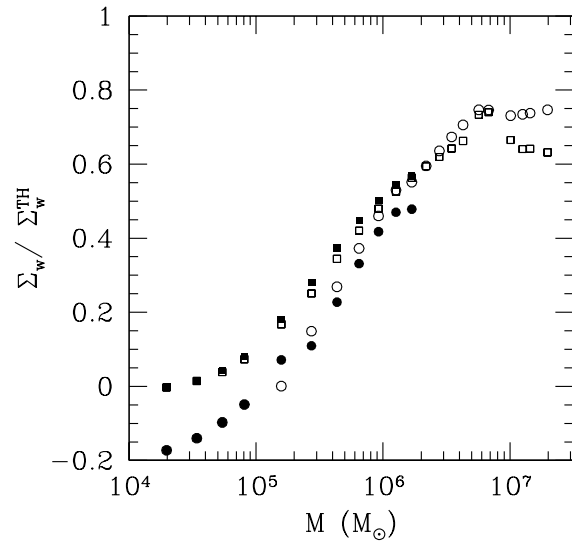


Figure 14. Ratio of the equivalent width weighted cross section for emission against the CMB for the hydrodynamical models to the cross sections for the tophat model, as a function of halo mass for haloes collapsing at $z_c = 10$ (squares) and $z_c = 20$ (circles). Shown for models including H_2 cooling (solid symbols) and without (open symbols).

overdensities near a collapsed halo. The equivalent width weighted cross section Σ_w^{obs} is only moderately affected by extending the integration volume beyond the core radius, as shown in Figure 12. Since the mean cosmic optical depth scales in proportion to this factor, as in Eq. (13), the surrounding gas is not expected to contribute much more to the mean cosmic optical depth.

The geometrically-averaged observed emission equivalent width is shown for a range of halo masses for haloes collapsing at $z_c = 10$ and 20 in Figure 13. The steep rise in the mean equivalent width with halo mass is partly a consequence of the mass scaling given by Eq. (29), but is also due to the mass dependence of the 21cm radiative efficiency η_{CMB} of the haloes. The more massive a halo, the greater its 21cm radiation efficiency for emission against the CMB.

Polynomial fits to the observer-frame equivalent-width weighted halo cross sections of the form $\Sigma_w^{\text{obs}} = \sum_{i=0}^4 a_i (\log_{10} M)^{4-i}$ are shown as well. The fits are performed for halo masses $\log_{10} M > 5$, below which Σ_w^{obs} is vanishingly small. Table 1 provides the coefficients for a range of collapse epochs. The fits may be used to interpolate the results of the hydrodynamical models on both the halo mass and the collapse epoch.

The ratios of the equivalent width from the hydrodynamical model to the tophat model for the haloes are shown in Figure 14. The scaling of the equivalent width with halo mass approaches the tophat prediction for the larger mass haloes. The average values from the hydrodynamical models are much smaller than the tophat prediction from Eq. (29) at the low mass end, where the haloes approach the Jeans mass and the gas becomes less overdense, as shown in Figure 3. The hydrodynamical values agree well with the tophat prediction at the high mass end despite the very different internal structures of the haloes. The smallest mass haloes actually produce a net absorption signal (cf. Figure 3).

4 COSMOLOGICAL 21CM SIGNATURE STATISTICS

4.1 Detection of minihaloes

The models neglect 21cm absorption or emission from the large-scale surroundings of the minihaloes. As primordial perturbations are intrinsically ellipsoidal (Bardeen et al. 1986), and flatten as they grow (Peebles 1980), modelling the region around a minihalo is not straightforward. Only in the late stage of collapse will a spheroidal system form. Nonetheless, it may be expected the infall region surrounding the minihalo may still be reasonably spherical.

The degree of spectral isolation of a minihalo may be estimated from the mean free path for intercepting a halo out to the turnaround radius. Approximating the space density of the haloes as $dn/d\log M$ gives a mean free path for interception of a typical halo of mass $0.9 \times 10^6 M_\odot$, with a comoving turn-around radius of 12.5 kpc, collapsing at $z_c = 8$ of 3.4 Mpc (comoving). The mean (observed) frequency separation of these systems is about 200 kHz. The detection of an individual absorption feature against a bright background source would require measuring the brightness temperature differential within frequency channels not much greater than 8 kHz, and preferably as narrow

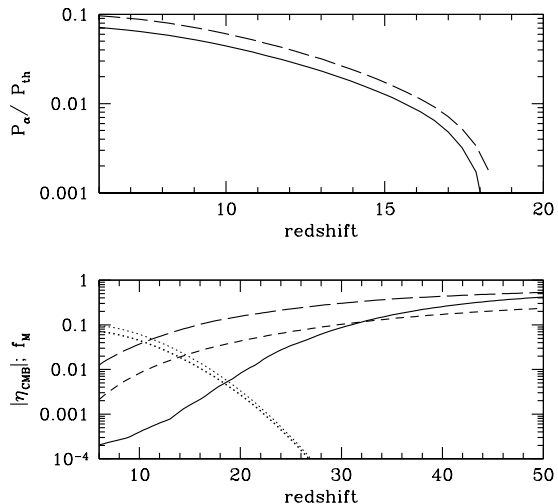


Figure 15. *Top panel:* Minimal Ly α photon collision rate, compared with the thermalization rate P_{th} , required for absorption against the CMB of the diffuse component of the IGM to exceed that from minihaloes, allowing for H₂ formation in the haloes (solid line) or not (dashed line). *Bottom panel:* The 21cm efficiency η_{CMB} for absorption or emission against the CMB from the diffuse component of the IGM due to H-H atomic collisions alone. For no heating (solid line), the IGM is in absorption, and dominates the minihalo contribution for $z > 19$. For an IGM temperature $T_K = 2T_{\text{CMB}}(z)$ (short-dashed line) and $10T_{\text{CMB}}(z)$ (long-dashed line), the diffuse IGM is in emission, and dominates the emission from minihaloes for $z > 15$. Also shown is the minihalo mass fraction f_M of the IGM, allowing for H₂ formation in the haloes (heavy dotted line), or not (light dotted line).

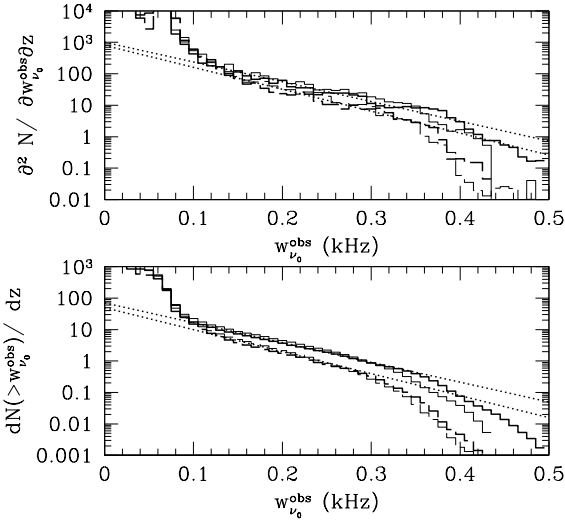
as 4 kHz or smaller to resolve the feature. For a spectral signal smoothed over broader frequency intervals comparable to the frequency separation of the features, the systems will produce a small modulation of the intensity step from the diffuse gas. For smoothing over much wider frequency intervals, it follows from Eq. (13) that the contribution from all systems will simply add a small constant amount to the overall intensity step from the diffuse gas.

It is noteworthy that at large redshifts absorption by gas beyond the turnaround radius diminishes Σ_w^{obs} somewhat for emission against the CMB, especially for small mass haloes. As shown in Figure 12, the asymptotic value of Σ_w^{obs} has not been reached for a $M = 0.8 \times 10^5 M_\odot$ halo collapsing at $z_c = 15$, so that the temperature differential may be somewhat over-estimated at these redshifts.

When the 21cm efficiency of the diffuse component of the IGM exceeds the mass fraction of the IGM in minihaloes, the diffuse IGM signal will overwhelm the minihalo signal. Given the mass range of minihaloes that contributes to the minihalo signal, it is possible to estimate the critical Ly α scattering rate required for the diffuse IGM signal to dominate. Using Eq. (16), and assuming a minimal halo mass given by M_{sh} and a maximum mass of M_{1000} , or $M_{1000}^{\text{noH}_2}$ if H₂ formation is suppressed, produces the critical scattering rates shown in Figure 15 (upper panel). Only a small

Table 1. Coefficients of $\Sigma_w^{\text{obs}}(M) = \Sigma_{i=0}^4 a_i (\log_{10} M)^{4-i}$ for emission against the CMB, for models without H₂ cooling. Units are kHz-kpc² (comoving).

z_c	a_0	a_1	a_2	a_3	a_4
6	1.5472	-31.916	247.88	-858.8	1119.9
8	2.0575	-43.378	344.21	-1217.9	1620.9
10	3.1682	-69.911	581.59	-2160.4	3021.4
15	5.6058	-128.130	1102.04	-4223.6	6081.3
20	6.7895	-156.428	1354.79	-5223.5	7559.6
30	6.2441	-146.889	1292.56	-5044.2	7366.8

**Figure 16.** Observed equivalent width distribution for absorption against a bright background source. *Top panel:* Shown are the differential distributions at $z = 8$ (solid lines) and $z = 10$ (dashed lines), with H₂ cooling (heavy lines) and without (light lines). The dotted lines show fits through the distributions with H₂ cooling. *Bottom panel:* The corresponding cumulative distributions.

fraction of the thermalization rate is required. In fact, for $z > 19$ collisions alone are sufficient to ensure absorption from the diffuse IGM dominates the signal from minihaloes (lower panel). In the presence of moderate amounts of heating, the diffuse IGM will dominate over minihaloes at even smaller redshifts. Shocks in the diffuse IGM may produce further emission against the CMB (Furlanetto & Loeb 2004; Kuhlen et al. 2006; Shapiro et al. 2006).

4.2 21cm statistics for absorption against a bright radio source

The most readily measured statistic of the minihalo 21cm signature against a bright background source is the equivalent distribution. The distributions at $z = 8$ and $z = 10$ from the hydrodynamical computations are shown in Figure 16. The cases with and without H₂ cooling have very similar distributions, except that for $z = 8$, the higher

mass haloes that survive with H₂ formation give rise to a slightly higher frequency of high equivalent width systems, with $w_{\nu_0}^{\text{obs}} > 0.32$ kHz, although these systems are rare.

The distributions are well-fit in the range $0.1 < w_{\nu_0}^{\text{obs}} < 0.3$ kHz by the exponential curves $\partial^2 N / \partial w_{\nu_0}^{\text{obs}} \partial z = N_0 \exp(-w_{\nu_0}^{\text{obs}} / w_*)$. At $z = 8$, $N_0 = 1400$ and $w_* = 0.069$ kHz, while at $z = 10$ $N_0 = 3100$ and $w_* = 0.062$ kHz, both for the case with H₂ cooling.

The distribution is dominated by very low mass haloes only for observed equivalent widths below $w_{\nu_0}^{\text{obs}} \lesssim 0.02$ kHz. Excluding sub-Jeans mass haloes, as given by Eq. (40), severely suppresses the number of absorption features for such small equivalent width values. By contrast, most of the effective optical depth from the haloes arises from sub-Jeans mass haloes. Excluding the contribution from sub-Jeans mass haloes results in an effective optical depth of $\tau_l \simeq 2.2 \times 10^{-4}$ for haloes collapsing at $z_c = 8$ for the case with H₂ cooling, a reduction by a factor of two compared with the case including the haloes.

4.3 21cm statistics for emission against the CMB

The evolution of the observed brightness temperature is shown in Figure 17. Since the emission equivalent width increases with the mass of the haloes, as shown in Figure 13, the extension to higher halo masses when H₂ formation is suppressed produces a doubling of the differential temperature compared with the case including H₂ cooling.

The effect of excluding the contribution of haloes with masses below the Jeans mass is also shown. At high redshifts these systems, although individually weak, are sufficiently abundant to contribute substantially to the minihalo signal.

The cumulative observed emission equivalent width distributions for haloes collapsing at $z_c = 8$ and 10 are shown in Figure 18. The heavy curves show the distribution including H₂ cooling and the light curves without. The extension to higher mass haloes in the latter case produces a higher frequency of larger equivalent width systems, although the distributions are found to extend to $w_{\nu_0}^{\text{obs}} > 5$ kHz for both cases. Numerous absorption systems with $-0.01 < w_{\nu_0}^{\text{obs}} < 0$ kHz arise as well for $z_c = 10$ resulting from absorption in the outer regions of the accreting haloes.

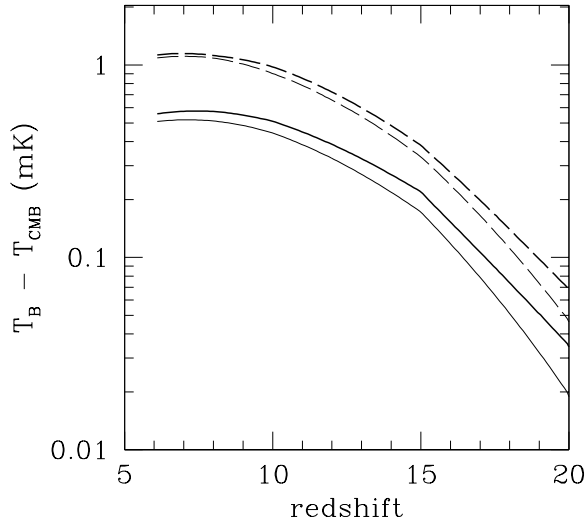


Figure 17. Observed brightness temperature differential relative to the CMB as a function of redshift, including H_2 cooling (solid line) and without (dashed line). The light lines corresponding to the heavy show the effect of excluding the contribution from haloes with masses below the Jeans mass of the gas.

5 DISCUSSION

5.1 21cm signature statistics

The 21cm signatures of minihaloes considered here, absorption against a bright background radio source and emission against the CMB, are dominated by haloes in different mass ranges. The absorption signal against a bright source is dominated by haloes in the approximate mass range $4.5 < \log_{10}(M/M_{\odot}) < 6$. The less massive haloes in this range lie below the Jeans mass, so that the post-infall gas pressure prevents as large an overdensity within the halo core from developing as in the more massive haloes. Haloes with masses above this range have a reduced absorption efficiency as a result of their higher post-shock temperatures. By contrast, the emission signature against the CMB increases with increasing halo mass, limited only by the maximum halo mass before star formation leads to the ejection of the halo gas.

As a consequence of their differing halo mass dependences, the signals will be affected differently by the various parameters defining the models. In this section, the role of some of these parameters in determining the strength of the signals is examined.

An issue only partially addressed in the minihalo approximation is the contribution of the surrounding moderately overdense gas on the overall signals. Minihaloes are not generally isolated structures, but are located within larger scale density inhomogeneities which themselves are non-linear. In the case of absorption against bright background sources, the overdense gas surrounding the collapsed minihalo was shown to contribute a small amount to the signal. Because of its near homogeneity in frequency, it could be

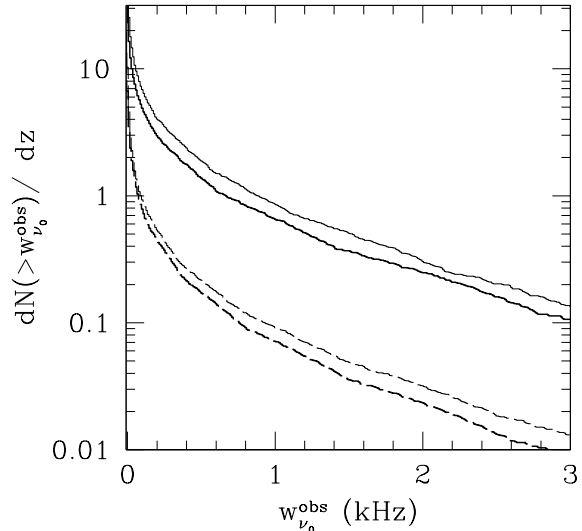


Figure 18. Observed equivalent width cumulative distribution for emission against the CMB at $z = 8$ (solid lines) and $z = 15$ (dashed lines), with H_2 cooling (heavy lines) and without (light lines).

readily subtracted off, leaving the equivalent width largely unaffected.

In the case of emission against the CMB, the role played by the surrounding gas is less clear. Beyond the central emitting minihalo, the gas is sufficiently dense and cool to act as an effective absorber against the CMB, cancelling in part the emission in an unresolved observation. If the absorbing region is sufficiently extensive, it could substantially reduce the net emission from minihaloes, as has been argued by Kuhlen et al. (2006) on the basis of numerical simulations. It is found here that extending the line-of-sight integration around the minihalo, although producing some reduction in the overall equivalent width, does not much reduce it. It is important to ensure the simulations adequately resolve the minihaloes in extended structures that would appear to be absorbing if under-resolved numerically. Achieving the required resolution in a simulation volume sufficiently large to represent a fair sample of the universe, without itself being overdense, is a formidable computational challenge. A possible solution is to model the statistical fluctuations surrounding the minihaloes semi-analytically.

5.2 Sensitivity to cosmological parameters

A prominent factor in establishing the strength of the signals is the primordial power spectrum. Both 21cm signatures are sensitive to the amount of power on small scales through their dependence on the halo mass distribution. Indeed, the signatures probe scales smaller than any current measurement of the primordial power spectrum, providing a potentially powerful means of constraining the shape of the primordial power spectrum and even the nature of dark matter.

In Figure 19, the predicted cumulative observed equiv-

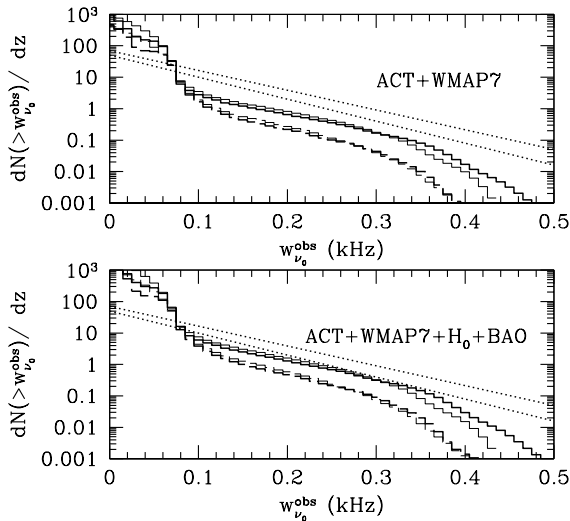


Figure 19. Cumulative observed equivalent width distributions for absorption against a bright background source, at $z = 8$ (solid lines) and $z = 10$ (dashed lines), with H_2 cooling (heavy lines) and without (light lines). *Top panel:* Cumulative distribution predicted for the best-fitting running spectral index model constrained by ACT and WMAP7 data. The dotted lines show the fit distributions with H_2 cooling for the fiducial cosmological model. *Bottom panel:* Cumulative distribution predicted for the best-fitting running spectral index model constrained by ACT, WMAP7, H_0 and BAO data.

alent width distributions for absorption against a bright background source are shown for the best-fitting cosmological models including a running spectral index found by combining WMAP Year 7 CMB data with the data from the Atacama Cosmology Telescope (ACT) (Dunkley et al. 2010). Two models are considered. The first is defined by the cosmological parameters $\Omega_m = 0.330$, $\Omega_v = 0.670$, $\Omega_b h^2 = 0.02167$, $h = 0.661$, $\sigma_{8h^{-1}} = 0.841$, spectral index at $k_0 = 0.002 \text{ Mpc}^{-1}$ of $n(k_0) = 1.032$, and slope $dn/d\log k = -0.034$. The second incorporates additional statistical priors based on measurements of the Hubble constant and Baryonic Acoustic Oscillations (BAOs), and is given by the cosmological parameters $\Omega_m = 0.287$, $\Omega_v = 0.713$, $\Omega_b h^2 = 0.02206$, $h = 0.691$, $\sigma_{8h^{-1}} = 0.820$, spectral index at $k_0 = 0.002 \text{ Mpc}^{-1}$ of $n(k_0) = 1.017$, and slope $dn/d\log k = -0.024$.

The suppression of power on small scales severely reduces the expected number of systems, by as much as two orders of magnitude for the first model. Including the constraints from H_0 and BAO measurements substantially increases the expected number of systems, but the numbers still lie well below the predictions for the fiducial cosmological model used in this paper. The counts of absorption systems would readily distinguish between the two running spectral index models, illustrating the power the 21cm detection of minihaloes has for constraining the small-scale primordial density power spectrum in the absence of other suppression mechanisms of the absorbers.

The reduced small scale power also reduces the pre-

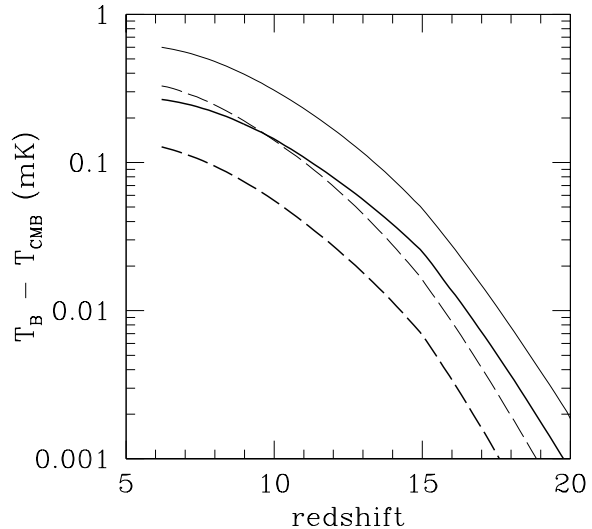


Figure 20. Observed brightness temperature differential relative to the CMB as a function of redshift, for cosmological models including a running spectral index. Shown are curves using models constrained by ACT and WMAP data with additional constraints from measurements of H_0 and BAOs (solid lines), and without (dashed lines), both for minihalo models including H_2 cooling (heavy lines) and without (light lines).

dicted temperature differentials from the CMB by factors of a few to several, as shown in Figure 20. Comparison with Figure 17 shows the reduction is particularly pronounced at high redshifts, where the signal is dominated by small mass haloes in the fiducial cosmological model that are suppressed in the models with a running spectral index. Measurements of the temperature differential especially at high redshift could thus readily constrain the running spectral index in the absence of other sources of suppression of the signal. It is noteworthy that a very weak signal at high redshifts compared with that expected in the fiducial model could be mistaken for a detection of cosmic reionisation in the absence of other observational constraints.

The halo mass dependence of the equivalent width for emission against the CMB given by Eq. (29) suggests the possibility of measuring the halo mass function directly from 21cm measurements. Whilst the hydrodynamical models produce a diminishing equivalent width with impact parameter, an observation with sufficient angular resolution to resolve the core of the structure could establish the central equivalent width value. The central value is shown as a function of halo mass in Figure 21. The equivalent width varies with the halo mass approximately as $w_{\nu_0} \sim M^{1.3}$. This is steeper than predicted for the tophat model. Nonetheless, the trend is sufficiently tight to yield a useful measurement of the halo mass.

The opposing mass dependences of the equivalent width as measured in absorption against a bright background source (BBS), Eq. (26), and the emission equivalent width in the tophat model suggests combining them may eliminate the dependence on halo mass, and yield a direct measure-

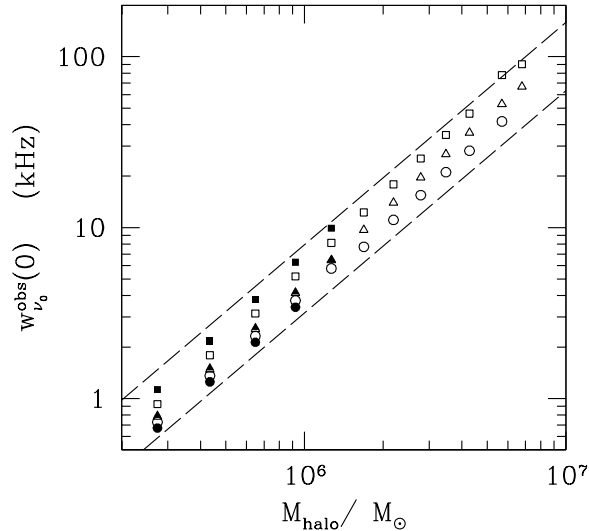


Figure 21. Observed central equivalent width for emission against the CMB as a function of halo mass, at $z = 10$ (squares), 15 (triangles) and 20 (circles). Results including H_2 cooling are shown as solid symbols; open symbols show results without H_2 cooling. The dashed lines show power laws $w_{\nu_0}^{\text{obs}} \sim M^{1.3}$.

ment of the combination of cosmological parameters given by

$$\left(w_{\nu_0}^{\text{obs}}\right)_{\text{BBS}} \left(w_{\nu_0}^{\text{obs}}\right)_{\text{CMB}} \simeq 4.42 \frac{(\Omega_b h^2)^2}{\Omega_m h^2} (\text{kHz})^2. \quad (46)$$

The ratio of equivalent widths eliminates the dependence on the baryon fraction, and would yield a measurement of the halo mass through

$$\left[\frac{(w_{\nu_0}^{\text{obs}})_{\text{CMB}}}{(w_{\nu_0}^{\text{obs}})_{\text{BBS}}}\right] \simeq 51(\Omega_m h^2)^{1/3} \left(\frac{M}{10^6 M_\odot}\right)^{2/3}. \quad (47)$$

In fact, dissipation breaks these relations. The actual relations both are mass dependent, and have no real advantage over inferring the mass from a measurement of the core equivalent width using the scaling relation shown in Figure 21. Probing the halo cores in emission against the CMB would, of course, be a formidable observational challenge.

5.3 Effects of first light

The far ultra-violet light from the first radiation sources in the Universe will redshift into local Ly α resonance line photons sufficiently distant from the sources. The scattering of the photons off the neutral hydrogen serves as a mechanism to decouple the spin temperature of the hydrogen from the CMB temperature through the Wouthuysen-Field effect (Wouthuysen 1952; Field 1958). Prior to reionisation, the intensity will grow sufficiently strong that the Ly α collision rate P_α will approach the thermalization rate P_{th} . For a cold IGM, with $T_K < T_{\text{CMB}}$, the 21cm optical depth will increase, increasing the absorption signature of minihaloes against bright background radio sources.

Well before the epoch of reionization, a small scattering rate $P_\alpha \ll P_{\text{th}}$ is expected. Whilst the photons will only slightly decouple the spin temperature from the CMB temperature, the vast reservoir of neutral hydrogen outside collapsed haloes will produce a sizeable absorption signature for an IGM colder than the CMB (Figure 15).

It is possible early sources will heat the IGM to temperatures above that of the CMB. Prior to reionisation, the primary heating mechanisms are through the photoelectric absorption of x-rays generated in shock-heated collapsed structures or possibly from any x-ray stellar sources or Active Galactic Nuclei (AGN) that have formed (Madau et al. 1997; Tozzi et al. 2000; Carilli et al. 2002; Furlanetto & Loeb 2004; Kuhlen et al. 2006), or by the scattering of higher order Lyman resonance line photons in the vicinity of their sources (Meiksin 2010). An increase in the IGM temperature will have two effects on the 21cm signatures: an increase in the minimum halo mass giving rise to a signal and the strength of the signal from individual haloes itself. The degree of the hydrodynamical effect on the haloes will depend on the specifics of the heating rate and history. In particular, as discussed in Section 3.1, the minimum halo mass required for the gas falling into the halo to shock and virialise increases. In lower mass haloes, the gas is heated by adiabatic compression, and the halo gas density profiles will adjust accordingly. The fraction of haloes affected will increase gradually with the increase in the IGM temperature.

By contrast, heating the IGM to a temperature above that of the CMB will produce a qualitative difference in both the absorption signature against a bright background radio source and emission against the CMB since for both cases, dislodging the spin temperature from the CMB temperature through either collisions or Ly α photon scattering will increase the spin temperature. To isolate this latter effect, the spin temperature is re-computed assuming an instantaneous boost of the IGM temperature by $\Delta T_K = 10T_{\text{CMB}}$, and the impact on the 21cm signatures assessed.

5.3.1 21cm signature against a bright radio source

The spin temperature for the hydrodynamical models is re-computed for five cases, having $P_\alpha/P_{\text{th}} = 0.001, 0.01, 0.1, 1$ and 10. Figure 22 shows typical profiles through a halo of mass $M = 0.9 \times 10^6 M_\odot$ collapsing at $z_c = 10$, including H_2 cooling, at a (comoving) projected separation from the halo centre of $b_\perp = 0.9$ kpc, corresponding to an observed equivalent width $w_{\nu_0}^{\text{obs}} = 0.20$ kHz for $P_\alpha = 0$. For $P_\alpha = 0.1P_{\text{th}}$, the equivalent width is only slightly reduced. For $P_\alpha = P_{\text{th}}$, the equivalent width is nearly halved, to 0.11 kHz. The profile is distorted into one having two minima, suggestive of two overlapping features. This arises from an enhanced contribution from the outflowing gas beyond the turn-around radius, as shown in Figure 23. Most of the absorption at $\nu - \nu_0 = 1$ kHz arises from infalling gas near the centre of the halo ($x_{\text{los}} < 12.5$ kpc), however the Doppler boosted absorption by outflowing gas also contributes. Whilst the contribution from the outflowing gas is small for $P_\alpha = 0$, for which the spin temperature is coupled to the CMB temperature, for $P_\alpha = P_{\text{th}}$ the spin temperature is coupled to the much colder IGM temperature, enhancing the net absorption to beyond that at line centre.

At still larger projected separations, referencing the

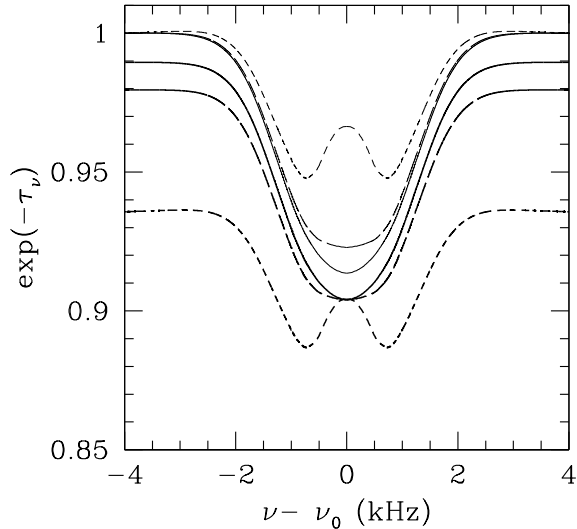


Figure 22. Absorption line profiles through a $0.9 \times 10^6 M_\odot$ halo collapsing at $z_c = 10$ at a projected separation from the halo centre of $b_\perp = 0.9$ kpc (comoving), corresponding to an observed equivalent width $w_{\nu_0}^{\text{obs}} = 0.20$ kHz for $P_\alpha = 0$. The profiles are for $P_\alpha/P_{\text{th}} = 0$ (solid lines), 0.1 (long-dashed lines) and 1 (short dashed lines). The profiles relative to the background level at $\nu - \nu_0 = 4$ kHz are shown as light curves. The frequency offset is in the observed frame.

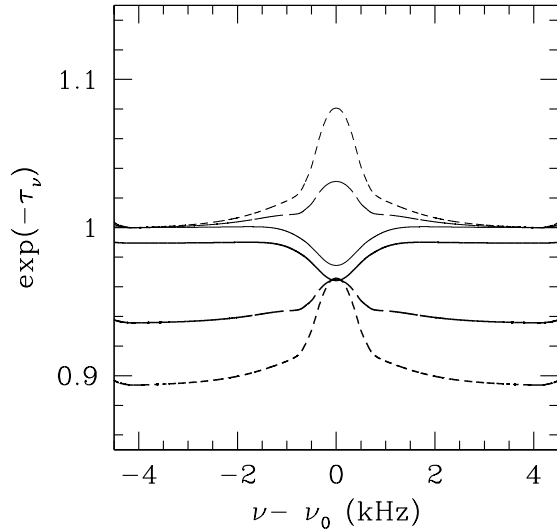


Figure 24. Absorption line profiles through a $0.9 \times 10^6 M_\odot$ halo collapsing at $z_c = 10$ at a projected separation from the halo centre of $b_\perp = 5.9$ kpc (comoving), corresponding to an observed equivalent width $w_{\nu_0}^{\text{obs}} = 0.030$ kHz for $P_\alpha = 0$. The profiles are for $P_\alpha/P_{\text{th}} = 0$ (solid lines), 1 (long-dashed lines) and 10 (short dashed lines). The profiles relative to the background level at $\nu - \nu_0 = 4$ kHz are shown as light curves. For $P_\alpha \geq P_{\text{th}}$, the profiles would appear as emission features against the background absorption level. The frequency offset is in the observed frame.

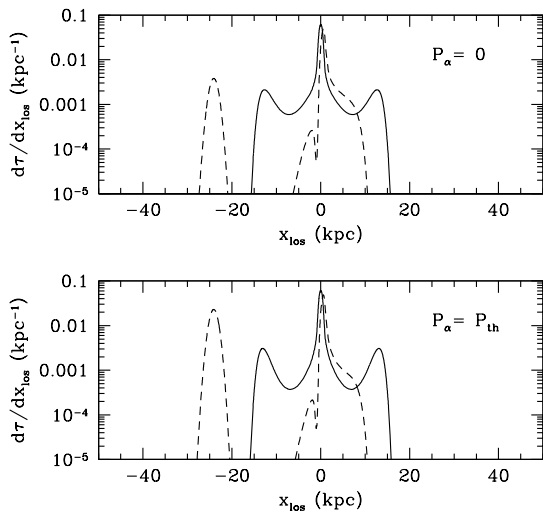


Figure 23. The differential optical depth $d\tau/dl$ per unit comoving length along the line of sight (in comoving kpc) through a $0.9 \times 10^6 M_\odot$ halo collapsing at $z_c = 10$ at a projected separation from the halo centre of $b_\perp = 0.9$ kpc (comoving), shown for frequency offsets $\nu - \nu_0 = 0$ (solid lines) and 1 kHz in the observed frame. *Top panel:* $P_\alpha = 0$. *Bottom panel:* $P_\alpha = P_{\text{th}}$.

background continuum to the value at 4 kHz results in positive apparent “emission” features for sufficiently large P_α , as shown in Figure 24. A line of sight through the halo above at $b_\perp = 5.9$ kpc corresponds to $w_{\nu_0}^{\text{obs}} \simeq 0.030$ kHz for $P_\alpha = 0$. For $P_\alpha = P_{\text{th}}$, the absorption feature would appear as an emission line with $w_{\nu_0}^{\text{obs}} \simeq 0.050$ kHz relative to the background absorption level at $\nu - \nu_0 = 4$ kHz. For $P_\alpha = 10P_{\text{th}}$, the feature would have $w_{\nu_0}^{\text{obs}} \simeq 0.12$ kHz. Such strong mock emission lines against a bright background source would be a tell-tale signature of an intense Ly α background radiation field and a cold IGM.

For a Ly α scattering rate as large as the thermalization rate, the optical depth increases substantially in the absence of heating, since the IGM temperature is much lower than that of the CMB. As a consequence, weak absorption features along the lines of sight adjacent to low mass haloes become substantially enhanced, resulting in a large number of absorbers. The observed equivalent width cumulative distributions for haloes collapsing at $z_c = 10$ are shown in Figure 25 for $P_\alpha = P_{\text{th}}$ and $P_\alpha = 10P_{\text{th}}$ (top panel). (The equivalent widths are computed using the intensity at a frequency offset of 2 kHz instead of 4 kHz as the continuum value due to limitations imposed by the volume of the hydrodynamical computations for such high absorption optical depths when $P_\alpha > P_{\text{th}}$.) The distributions are only representative, as features will be produced by much more moderate density fluctuations throughout the IGM, not only in the vicinity of haloes. They indicate, however, the large numbers of features that would arise in a cold IGM.

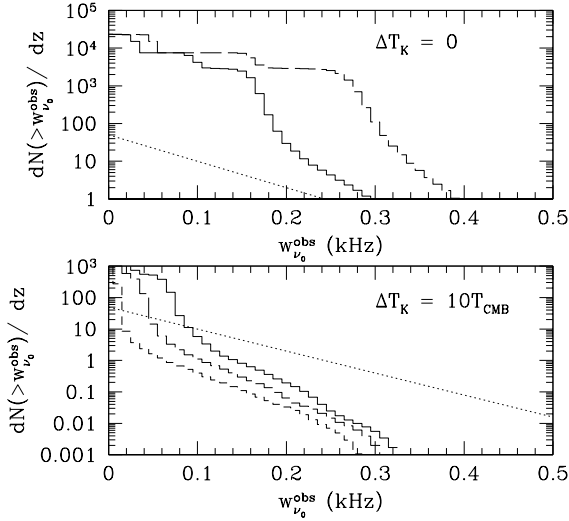


Figure 25. Cumulative observed equivalent width distributions for absorption against a bright background source from haloes collapsing at $z_c = 10$, including H_2 cooling. *Top panel:* The curves correspond to $P_\alpha = P_{th}$ (solid line) and $P_\alpha = 10P_{th}$ (dashed line). *Bottom panel:* The spin temperatures are computed including a temperature boost by $10T_{CMB}(z_c)$. The curves correspond to $P_\alpha/P_{th} = 0$ (solid line), 1 (long-dashed line) and 10 (short-dashed line). In both panels, the dotted line shows the fit distribution with H_2 cooling for $P_\alpha = 0$ and no boost in the IGM temperature.

The mean free path between haloes corresponding to absorption features with observed equivalent widths $w_{\nu_0}^{obs} < -0.05$ kHz and $w_{\nu_0}^{obs} > 0.2$ kHz and 0.4 kHz are shown in Figure 26 (top panel). Systems with $w_{\nu_0}^{obs} > 0.2$ kHz arise predominantly from low mass haloes, with a flat contribution over the range $10^4 - 10^5 h^{-1} M_\odot$. Mock emission systems, with $w_{\nu_0}^{obs} < -0.05$, arise from the outer regions of more massive haloes with masses $6 - 9 \times 10^5 h^{-1} M_\odot$.

In an IGM in which P_α was fluctuating, patches with P_α exceeding P_{th} would show up as regions with a highly dense 21cm forest. Similarly, if P_α exceeded P_{th} throughout the IGM while reionization and pre-reionization heating were still incomplete, patches with low T_K would produce a highly dense 21cm forest.

The effect of allowing for a temperature boost $\Delta T_K = 10T_{CMB}$ in the IGM on the absorption equivalent width distribution is shown in Figure 25 (bottom panel) for $P_\alpha = 0$, P_{th} and $10P_{th}$. The effect is to severely reduce the expected number of systems with $w_{\nu_0}^{obs} > 0.1$ kHz. Weaker features arise predominantly from the peripheries of haloes in the mass range $2 - 5 \times 10^5 h^{-1} M_\odot$, as shown in Figure 26 (bottom panel). The mean free path for a feature with $w_{\nu_0}^{obs} > 0.2$ kHz increases from $\lambda_{mfp} \simeq 60 h^{-1}$ Mpc (comoving) for $\Delta T_K = 0$ and $P_\alpha = 0$, as shown in Figure 10, to $\lambda_{mfp} \simeq 200 h^{-1}$ Mpc (comoving) or larger. The signal is dominated by haloes with a mass $M \simeq 3 \times 10^5 h^{-1} M_\odot$. Weaker systems, with $w_{\nu_0}^{obs} > 0.1$ kHz, arise primarily from lower mass haloes, with $1 - 5 \times 10^5 h^{-1} M_\odot$, for $P_\alpha = 0$, whilst for $P_\alpha = P_{th}$,

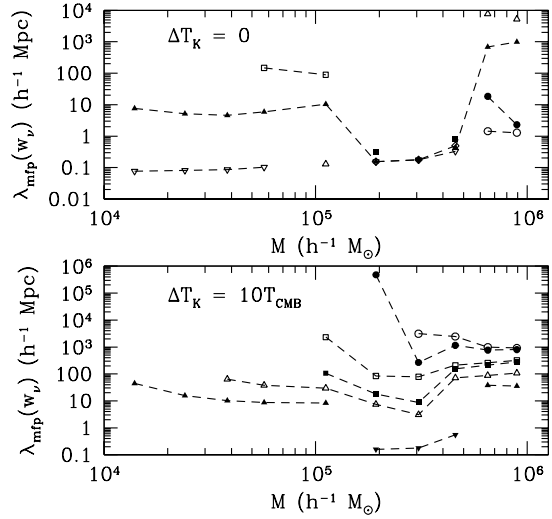


Figure 26. Comoving mean free path for haloes collapsing at $z_c = 10$ giving rise to absorption features against a bright background source. *Top panel:* The mean free path for $P_\alpha = P_{th}$ (solid symbols) and $P_\alpha = 10P_{th}$ (open symbols), corresponding to absorption systems with observed equivalent widths $w_{\nu_0}^{obs} < -0.05$ kHz (circles), $w_{\nu_0}^{obs} > 0.2$ kHz (triangles; upper limits shown as inverted triangles) and $w_{\nu_0}^{obs} > 0.4$ kHz (squares). *Bottom panel:* The mean free path for haloes, adjusting the spin temperature by adding $10T_{CMB}$ to the kinetic temperature of the gas. Shown for $P_\alpha = 0$ (solid symbols) and $P_\alpha = P_{th}$ (open symbols), corresponding to absorption systems with observed equivalent widths $w_{\nu_0}^{obs} > 0.05$ kHz (triangles; upper limits shown as inverted triangles), $w_{\nu_0}^{obs} > 0.1$ kHz (squares) and $w_{\nu_0}^{obs} > 0.2$ kHz (circles).

the signal is dominated by a nearly flat contribution from haloes with masses $2 \times 10^5 M_\odot - 10^6 h^{-1} M_\odot$.

The dynamical impact of the temperature boost would be moderate on the signature. From Eq. (37), the boost in temperature would unbind the gas in haloes with masses smaller than $2 \times 10^5 h^{-1} M_\odot$, corresponding to absorption features with $w_{\nu_0}^{obs} < 0.1$ kHz. Of course a larger temperature boost would suppress stronger features.

5.3.2 21cm signature against the CMB

The scattering of $Ly\alpha$ photons weakens the 21cm emission signature from minihaloes against the CMB as the spin temperature couples increasingly strongly to the lower kinetic temperature of the diffuse IGM. In Figure 27, the brightness temperature signature is shown for $P_\alpha/P_{th} = 0, 0.01, 0.1$ and 1. The corresponding observed equivalent widths are 9.8, 4.1, -42 and -270 Hz, integrating between $\nu - \nu_0 = \pm 4$ kHz. The signal is halved for $P_\alpha/P_{th} = 0.01$, and produces a net absorption signature for $P_\alpha/P_{th} = 0.1$ and larger.

In fact the equivalent width of an individual halo is no longer well-defined, since the entire IGM becomes absorbing. From Eq. (13), the strength of the overall signature depends on the equivalent width weighted cross-section Σ_w^{obs} .

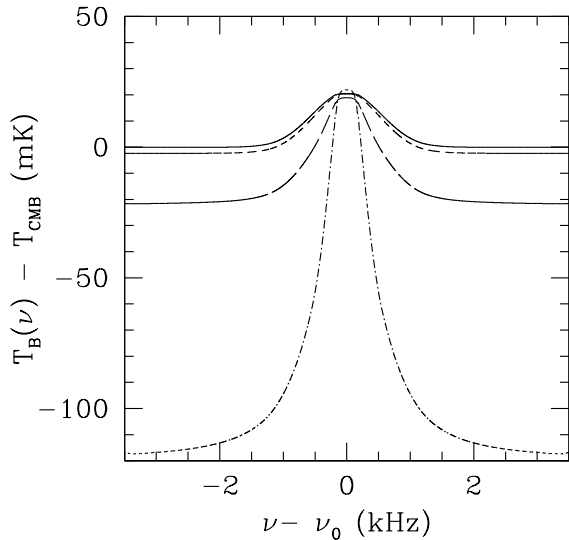


Figure 27. The observed brightness temperature relative to the CMB along the line of sight at a projected radius $b_{\perp} = r_c$ for a halo of mass $M = 0.9 \times 10^6 M_{\odot}$ collapsing at $z_c = 15$, for $P_{\alpha}/P_{\text{th}} = 0$ (solid line), 0.01 (short-dashed line), 0.1 (long dashed line), and 1 (dot-dashed line). The emission signature converts into a net absorption signature by $P_{\alpha}/P_{\text{th}} = 0.1$. The frequency offset from line centre is in the observed frame.

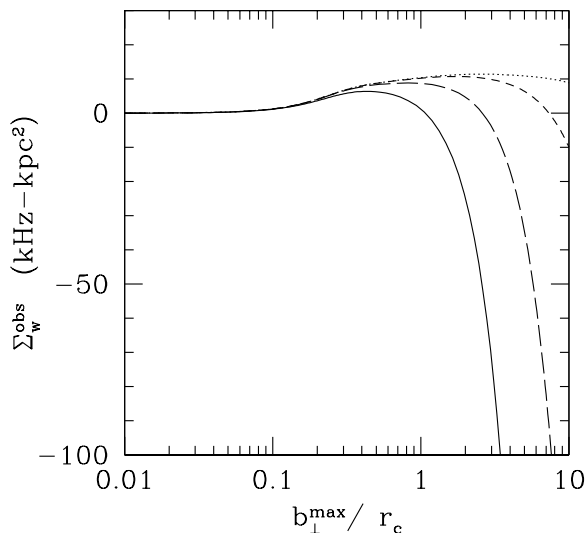


Figure 28. Observed integrated equivalent width weighted co-moving cross section for emission against the CMB as a function of comoving maximum impact parameter b_{\perp}^{max} , normalized by the core radius. Shown for a halo of mass $M = 0.9 \times 10^6 M_{\odot}$ collapsing at $z_c = 15$, for $P_{\alpha}/P_{\text{th}} = 0.001$ (dotted line), 0.01 (short-dashed line), 0.1 (long-dashed line) and 1 (solid line).

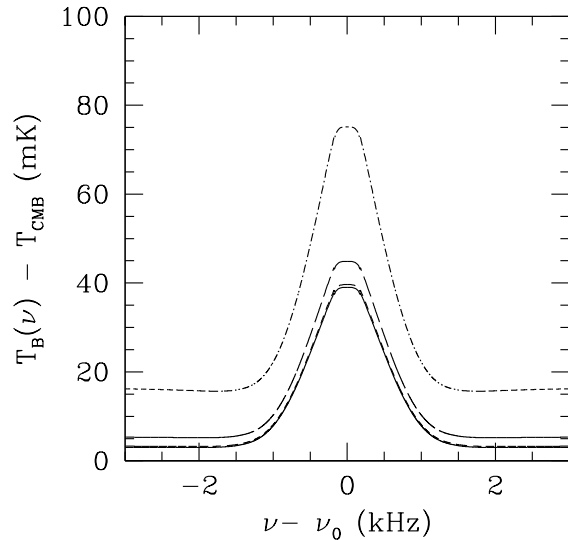


Figure 29. The observed brightness temperature relative to the CMB along the line of sight at a projected radius $b_{\perp} = r_c$ for a halo of mass $M = 0.9 \times 10^6 M_{\odot}$ collapsing at $z_c = 15$ and including a boost in the IGM temperature by $\Delta T_K = 10T_{\text{CMB}}$, for $P_{\alpha}/P_{\text{th}} = 0$ (solid line), 0.01 (short-dashed line), 0.1 (long dashed line), and 1 (dot-dashed line). The growing wings arise from the increase in the IGM emission as P_{α} increases. The frequency offset from line centre is in the observed frame.

Except for very small values $P_{\alpha}/P_{\text{th}} \ll 1$, even if the minihalo contribution were defined by restricting the frequency range for evaluating the equivalent width to ± 4 kHz of the line centre, Σ_w^{obs} is again not well-defined for an individual halo. As shown in Figure 28, averaging over increasingly large maximum impact parameters produces an increasingly negative value even for P_{α}/P_{th} as small as 0.01. The emission signal from the minihalo is swamped by the absorption from the surrounding cold IGM. Indeed, on larger scales absorption from the diffuse IGM is expected to dominate, as shown in Figure 15. For even small values of P_{α}/P_{th} , the minihalo model is no longer an effective approximation for estimating the signature of the IGM against the CMB. If a direct signal from the minihaloes may be detected at all, it would only be from high angular resolution measurements that were able to resolve individual minihaloes. This would require sub-arcsecond beam angles, well beyond the specifications of currently existing or planned radio facilities for the foreseeable future.

It is possible that the $\text{Ly}\alpha$ scattering rate would be suppressed within dusty regions produced by winds from galaxies, as the $\text{Ly}\alpha$ photons would be absorbed along their long path lengths as they re-scatter. In the vicinity of a bright galaxy, however, the scattering of higher order Lyman resonance line photons alone would be adequate to produce a net absorption signature from nearby minihaloes. Typical scattering rates of $P_n/P_{\text{th}} \simeq 0.001 - 0.01$ for $\text{Ly}-n$ photons are expected (Meiksin 2010).

Boosting the IGM temperature by $\Delta T_K = 10T_{\text{CMB}}$ gives rise to an emission signature from the diffuse IGM, which produces a wing on the minihalo emission line, as

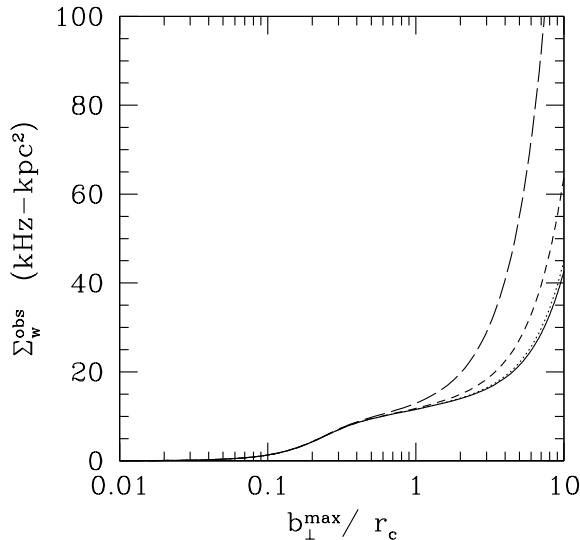


Figure 30. Observed integrated equivalent width weighted comoving cross section for emission against the CMB as a function of comoving maximum impact parameter b_{\perp}^{max} , normalized by the core radius. Shown for a halo of mass $\bar{M} = 0.9 \times 10^6 M_{\odot}$ collapsing at $z_c = 15$ with the IGM temperature instantaneously boosted by $\Delta T_K = 10 T_{\text{CMB}}$, for $P_{\alpha}/P_{\text{th}} = 0$ (solid line), 0.01 (dotted line), 0.1 (short-dashed line) and 1 (long-dashed line).

shown in Figure 29. A substantial emission wing is found even for $P_{\alpha} = 0$. The collisional coupling to the gas kinetic temperature alone is sufficient to produce the wing (cf. Figure 15). Even when the frequency range for evaluating the equivalent width is restricted to within 4 kHz of the line centre, the equivalent width weighted cross-section Σ_w^{obs} is found not to converge with increasing impact parameter out to at least a few times the turnaround radius, as shown in Figure 30. Whilst there is a quasi-convergence for $b_{\perp} \simeq r_c$, averaging over larger values results in a diverging quantity. The emission signal from the surroundings of the halo swamps that of the minihalo contribution from $b_{\perp} < r_c$. The minihalo model is again no longer a useful approximation for quantifying the contribution to the total temperature differential $T_B - T_{\text{CMB}}$, now dominated by the contribution from the diffuse IGM beyond the core radius of the minihalo.

5.3.3 Combined 21cm signatures

The impact of the first radiation sources on the joint 21cm signals from the IGM prior to reionisation is divided into six broad regimes: (a) $\Delta T_K \ll T_K$, $P_{\alpha} \ll \ll P_{\text{th}}$; (b) $\Delta T_K < T_{\text{CMB}} - T_K$, $P_{\alpha} \ll \ll P_{\text{th}}$; (c) $\Delta T_K < T_{\text{CMB}} - T_K$, $0.01 P_{\text{th}} < P_{\alpha} \ll P_{\text{th}}$; (d) $\Delta T_K > T_{\text{CMB}} - T_K$, $P_{\alpha} \ll P_{\text{th}}$; (e) $\Delta T_K \ll T_K$, $P_{\alpha} > P_{\text{th}}$; and (f) $\Delta T_K > T_{\text{CMB}} - T_K$, $P_{\alpha} > P_{\text{th}}$. The differences in behaviour between the absorption against bright background radio sources and the signal against the CMB may be exploited to distinguish the factors of heating, Ly α scattering and the uncertain amount of power on small scales.

In regime (a), absorption by minihaloes against a bright background radio source and emission against the CMB is unaffected by galactic feedback. (By $P_{\alpha} \ll \ll P_{\text{th}}$ is meant a Ly α scattering rate well below that required to increase the 21cm efficiency of the diffuse component of the IGM to above the mass fraction of the IGM in minihaloes. See Figure 15.) The redshift evolution of the signals traces the growth of structures on comoving scales down to a few kiloparsecs. In regime (b), the absorption signal against a bright background source weakens whilst the minihalo signal against the CMB is largely unaffected. Although the signal from shocked gas in the diffuse IGM may evolve somewhat, it may be possible to isolate the development of large-scale structure using the signal against the CMB from the effects of heating on the absorption systems against bright sources. In regime (c), the signal from the absorption systems weakens as in regime (b), but the signal against the CMB now goes into deep absorption. This would indicate the presence of a moderate metagalactic UV radiation field. Disentangling the effects of heating, Ly α scattering and small-scale power would be difficult. In regime (d), the absorption against a bright background source continues to diminish as the IGM is warmed, but the signal against the CMB goes into strong emission, which continues to strengthen as either ΔT_K or P_{α} increases until the signal saturates with full emission from the IGM against the CMB. Before saturation, joint modelling of the signal against bright sources and against the CMB may partially disentangle the effects of heating, Ly α scattering and small-scale structure growth as an increasing P_{α} has little effect on the absorption systems but a strong effect on the emission signal against the CMB once $P_{\alpha} > 0.01 P_{\text{th}}$. In regime (e), the absorption signal against background sources becomes very strong, producing a large number of absorption systems, whilst the signal from the minihaloes and their environs against the CMB will go strongly into absorption. The large number of absorbers indicates little heating so that its strength is determined primarily by the Ly α scattering rate and the amount of small-scale power. In regime (f), the absorption signal from the minihaloes against a bright background source will be diminished, with a large contribution arising from the diffuse IGM. The diffuse IGM signal against the CMB will be in emission and saturate for a sufficiently large Ly α scattering rate. The minihalo signal against the CMB will be overwhelmed by the emission from the diffuse component.

5.4 Effects of reionisation

The collapsed haloes achieve large central hydrogen densities and large central H I column densities, with values $N_{\text{H}} > 10^{20} \text{ cm}^{-2}$ typical. The haloes will be detectable into the Epoch of Reionisation, although with reduced cross-sections as their outer regions become heated and photoionised by the ambient UV radiation field. The degree of reduction depends on the intensity of the radiation field.

Two simple limiting cases are considered for estimating the incident flux of ionising photons. The emissivity necessary for reionising the Universe may be minimally estimated by requiring one photon per hydrogen atom over a Hubble time. If clumping drives the mean hydrogen recombination time to under a Hubble time, then the emissivity may be estimated instead by requiring one photon per mean hydro-

gen recombination time. The column density required for shielding the interior of the halo from the incident flux may then be estimated by modelling the ionisation zone within the halo as an inverted Strömgen sphere.

The minimal flux based on one photon per baryon is $\langle n_{\text{H}}(z) \rangle c$, where the angle brackets indicate spatial averaging over the IGM. If the radiation field penetrates to a depth l within the halo, balancing recombinations with ionisations within the ionised surface layer gives $l \simeq \langle n_{\text{H}}(z) \rangle c / n_{\text{H},c}^2 \alpha_B$, where $n_{\text{H},c}$ is the internal hydrogen density of the halo and α_B the radiative recombination rate (Case B) within the ionised zone. A density of $n_{\text{H},c} = f_c^{-3} \langle n_{\text{H}} \rangle$ and a temperature of 10^4 K in the ionised layer gives $N_{\text{H}} = n_{\text{H},c} l = c f_c^3 / \alpha_B \simeq 6 \times 10^{20} \text{ cm}^{-2}$ for $f_c = 1/(18\pi^2)^{1/3}$. Since the density rapidly rises within the collapsed halo to higher values, the required column density will be somewhat smaller, depending on the mass of the halo and collapse epoch.

If the clumpiness of the IGM is sufficiently large, the reionisation will be recombination limited. In this case the incident flux of ionisation radiation is $\langle n_{\text{H},c}^2 \rangle \alpha_B c / H(z)$. If the clumping factor of the IGM is dominated by the haloes, then balancing recombinations within the outer ionisation layer of a halo with the ionisation rate gives a depth for the ionisation layer of $l = f_V c / H(z)$, where f_V is the volume filling factor of the haloes. For collapsed tophat haloes, this is related to the mass fraction f_M in collapsed haloes by $f_V = f_c^3 f_M$. The column density of hydrogen through the ionised layer is then $N_{\text{H}} = f_M n_{\text{H}}(z) c / H(z) \simeq 10^{22} \text{ cm}^{-2}$ at $z = 10$, adopting f_M from Figure 15. This means the ionising radiation would be able to penetrate deeply into the core, much reducing the cross section, but still not eliminating all the haloes from detection.

5.5 Departure from self-similar accretion

The characteristic infall velocity and temperature of the post-shock halo gas predicted from Eqs. (35) and (36) scale as power laws of the halo mass. Self-similar accretion may then be expected, as is the case for cosmological infall of a self-gravitating initially pressureless collisional gas (Bertschinger 1985). A departure from self-similarity, however, is produced by the outer boundary condition of a finite IGM temperature, and so a non-vanishing pressure. Whilst for more massive haloes the IGM pressure may be neglected, the pressure results in a non-negligible contribution to the post-shock temperature in a minihalo.

The jump condition for the temperature for an adiabatic shock is $T_2/T_1 = [2\gamma\mathcal{M}_1^2 - (\gamma - 1)][(\gamma - 1)\mathcal{M}_1^2 + 2]/[(\gamma + 1)^2\mathcal{M}_1^2]$ for a gas with ratio of specific heats γ , where $\mathcal{M}_1 = |v_1|/c_1$ is the mach number for the inflowing gas with velocity v_1 (relative to the shock front) and adiabatic sound speed c_1 . For an initially pressureless gas, the shock is always very strong and the post-shock temperature depends only on the gas velocity, as in Eq. (36). For gas starting at the intergalactic temperature, adiabatic compression will pre-warm the gas by a factor of up to f_c^{-2} , as given by Eq. (38). This results in a mild shock rather than a strong shock, with the strength of the shock increasing with the halo mass, as shown in Figure 31. For the larger masses, the post-shock temperature approaches the strong shock limit T_{sh} of Eq. (36) at about half the (proper) collapse radius $r_c = f_c r_0 / (1 + z_c)$.

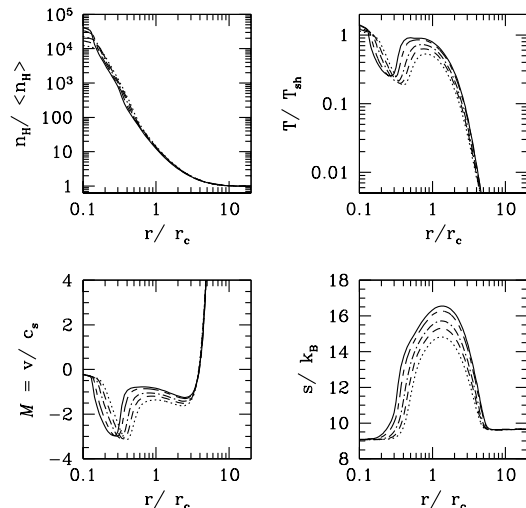


Figure 31. Fluid variables for haloes collapsing at $z_c = 20$ for halo masses $\log_{10} M = 6.44$ (dotted line), 6.54 (dashed line), 6.63 (dot-dashed line), 6.76 (short-dashed-long-dashed line), and 6.83 (solid line), for a tophat spherical perturbation, with H_2 cooling suppressed. Shown are the normalised hydrogen density (top left panel), gas temperature (top right panel), fluid velocity expressed as a Mach number (bottom left panel), and entropy per particle (in units of k_B) (bottom right panel). The peak value of $T(r)/T_{\text{sh}}$ and the entropy increase with halo mass.

For the example shown in Figure 7 (solid curves in Figure 31), the gas becomes self-gravitating as the gas continues to flow inward, with a baryonic mass of $7 \times 10^5 M_{\odot}$ in the inner 0.8 kpc (comoving) by $z = 20.1$, about 50 times the dark matter mass. As the gas comes to rest at the centre of the halo, the gas develops a steep central density profile. The further compression in the time-varying potential results in a further boost in the gas temperature, until values somewhat above T_{sh} are reached at the centre. In more massive haloes, temperatures approaching, and in some cases even somewhat exceeding, the virial temperature are reached, driving the gas into a rapid cooling phase through $\text{Ly}\alpha$ excitation, which will ultimately result in star formation. More than $10^3 M_{\odot}$ of stars form within the core by $z = 20$. The resulting supernovae will likely expel the gas from the minihalo. A cosmological simulation code unable to resolve the inner few hundred parsecs (comoving) would fail to detect the cooling instability that develops in the centre of the halo, and treat the halo as stable.

One caveat in the solution is that the inverted entropy profile may result in a convective instability outside the core. As discussed in Sec. 3.3 above, the growth time is typically longer than the lifetime of massive stars, so that the halo will be disrupted before the instability sets in. This will not be the case, however, for haloes of too small mass to form stars. As shown in Figure 32, the Brunt-Väisälä timescale is shorter than 100 Myr just outside the core radius for the more massive haloes less massive than the critical mass $\log_{10} M = 6.1$ for which more than $10^3 M_{\odot}$ of stars

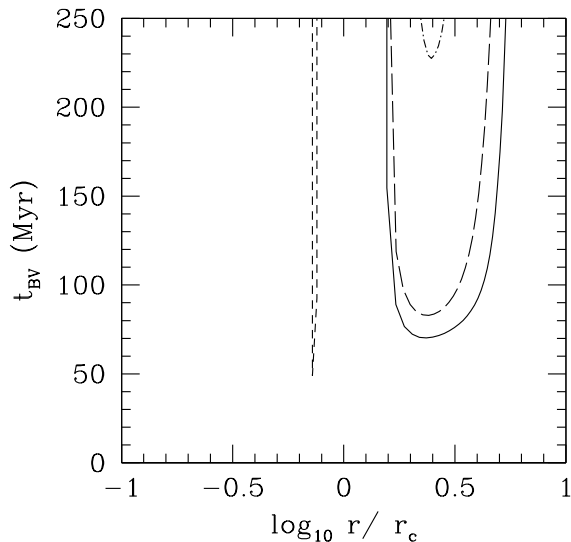


Figure 32. Brunt-Väisälä growth time for convective instability for haloes collapsing at $z_c = 20$ at $z = 20$. Shown for haloes of mass $\log_{10} M = 4.73$ (short-dashed line), 5.20 (dotted-dashed line), 5.64 (long-dashed line) and 6.00 (solid line), as a function of radius, normalised by the core radius $r_c(M)$.

form from H_2 cooling. For the case $\log_{10} M = 4.73$, close to the Jeans mass, the gas becomes convectively unstable just within the core. If the timescale is shorter than the typical time between mergers, the halo would become convectively unstable. In this case, the halo gas would fragment, possibly bringing on a contraction of the halo, diminishing the number of systems detected per unit redshift. A high resolution 3D simulation would be required to assess the effect of the instability.

A second caveat is that the baryons will draw in the dark matter into the central region, an effect not included here. As a consequence, the hydrodynamical flow of the gas must be included to describe the dark matter halo profile on sub-kiloparsec (comoving) scales. The increase in the amount of dark matter will strengthen the gravitational field in the centre of the halo, and enhance the cooling instability.

5.6 Comparison with previous results

Fluctuations in the 21cm signature are an expected consequence of the large-scale structure of the dark matter and baryons in the Universe (Hogan & Rees 1979; Tozzi et al. 2000). The 21cm forest from small-scale cosmological structures was extracted from numerical reionization simulations by Carilli et al. (2002). The IGM was heated by the reionizing radiation to a volume-averaged temperature well above that of the CMB, and had a baryonic mass per particle of at best $\log_{10} M = 5.7$. The masses of the resolvable dark matter haloes would be over two orders of magnitude larger, exceeding the upper mass limit before stars would form. Most of the features in the simulated spectra in fact arose from moderately overdense filaments, the gas within which will not have been well-resolved into the minihaloes

that give rise to the 21cm features. The simulations were also carried out in boxes too small to provide fair samples of the universe. The simulations nonetheless clearly established the viability of detecting the 21cm forest in the spectra of bright background radio sources.

To overcome some of the limitations of simulations, Furlanetto & Loeb (2002) modelled the minihaloes as spheres in hydrostatic equilibrium within a dark matter halo with a static isothermal core at the halo virial temperature and an infalling outer region at the IGM temperature extending to the turn-around radius, beyond which the sphere parameters were adjusted to match onto the diffuse IGM. The IGM temperature from Carilli et al. (2002) was adopted; at $z = 10$ the temperature is 1000 K. A model with an IGM temperature a factor ten lower was also considered. In both cases, the IGM temperature is above the CMB temperature. No models with an IGM temperature lower than that of the CMB were considered. They allow for minihaloes up to a mass corresponding to a virial temperature of 10^4 K. $Ly\alpha$ photon scattering rates of $P_\alpha/P_{th} \simeq 1$ and 10 at $z = 10$ were adopted, as well as $P_\alpha = 0$. They find $dN/dz \simeq 10$ for $w_{\nu_0}^{obs} \gtrsim 0.1$ kHz at $z = 10$ for their colder model with $P_\alpha \simeq P_{th}$. The model parameters correspond closely to those considered here with an IGM temperature boost and $P_\alpha = P_{th}$. For the model here, $dN/dz(w_{\nu_0}^{obs} > 0.1 \text{ kHz}) \simeq 1$, about an order of magnitude smaller. This may in part be due to the somewhat higher IGM temperature of 300 K for the boosted temperature model here, compared with 100 K for the model of Furlanetto & Loeb (2002). Their hotter model, with an IGM temperature of 1000 K, has $dN/dz(w_{\nu_0}^{obs} > 0.1 \text{ kHz}) \simeq 1$. In the model here, however, the line density declines faster for systems with $w_{\nu_0}^{obs} > 0.3$ kHz, for which $dN/dz \simeq 0.002$; Furlanetto & Loeb (2002) obtain 0.02, an order of magnitude larger. The difference may arise from the lower truncation in the upper minihalo mass imposed here, allowing for star formation following H_2 formation. Given the differences between the models, the overall agreement is reasonably good.

Using a static, non-singular, truncated isothermal sphere model with a temperature given by the virial temperature, and numerical simulations to estimate the halo number density, Shapiro et al. (2006) compute the expected 21cm emission from minihaloes assuming radiative feedback effects from the first light sources are negligible. They allow for halo masses having virial temperatures up to 10^4 K. At $z = 8$, they obtain a brightness temperature differential $\delta T_B = T_B - T_{CMB} \simeq 3.5$ mK at $z = 8$. Adjusting to their cosmological model parameters (similar to those assumed here, except the primordial power spectrum is untilted and normalized to $\sigma_{8h-1} = 0.9$), the tophat model for the same mass range predicts $\delta T_B \simeq 3.0$ mK, very close to their value. As shown in Figure 14, however, the tophat model generally exceeds the prediction from the dynamical minihaloes computed here. The dynamical halo model, with H_2 formation suppressed, predicts the smaller value of $\delta T_B \simeq 1.4$ mK, allowing for masses up until star formation occurs as given by Eq. (45). Using the tophat model to extend to the upper mass limit adopted by Shapiro et al. (2006) boosts this value to 1.9 mK. Given the differences between the models, this is reasonably good agreement. The weaker value found here, however, only slightly exceeds the value of 1.5 mK Shapiro et al. (2006) find for the emission from the diffuse

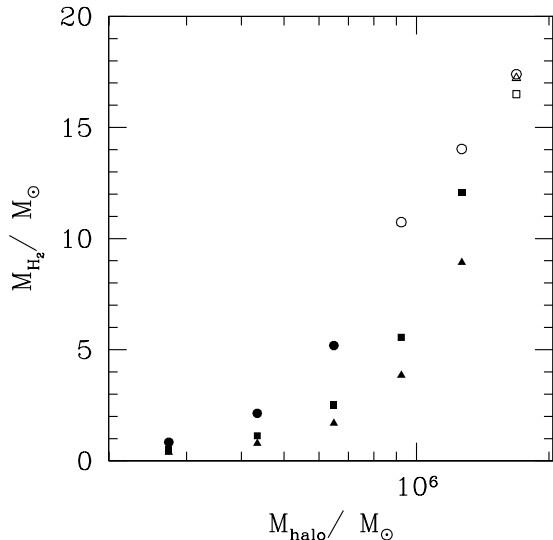


Figure 33. Mass in molecular hydrogen within the turn-around radius, as a function of total halo mass, at collapse epochs $z_c = 8$ (triangles), 15 (squares) and 30 (circles). Open symbols indicate haloes that formed more than $1000 M_\odot$ of stars by the time of their collapse.

IGM alone. Allowing for the lower upper mass limits obtained here suggests the emission from minihaloes is at most comparable to that of the diffuse IGM.

5.7 Implications for galaxy formation

The large densities in the cores of the minihaloes result in rapid cooling either through molecular hydrogen or collisional excitation of hydrogen. In the presence of molecular hydrogen cooling, the minimum halo mass for forming stars is found to range from 0.9 to $1.6 \times 10^6 M_\odot$ for $30 > z > 8$, declining to $0.4 \times 10^6 M_\odot$ at $z = 50$. The corresponding range of virial temperatures is $3700 - 1600$ K.

If molecular hydrogen is dissociated by the metagalactic UV radiation field from the first stars, as is argued by Haiman et al. (1997a) and Haiman et al. (2000), the minimum halo mass for cooling sufficiently to form stars increases to $3 \times 10^6 - 8 \times 10^6 M_\odot$ for $50 > z > 8$, corresponding to virial temperatures of $14000 - 4600$ K. This range extends the estimate of $10^{3.8}$ K given by Haiman et al. (2000).

Since the gas in the low mass minihaloes discussed here will be disrupted by the photoionisation and supernovae from the first stars, still more massive haloes able to maintain star formation would be required to reionize the IGM. The supernovae ejecta, however, will mix into the gas of more massive haloes as the smaller haloes merge during the progression of hierarchical clustering. The metals from these smaller systems will provide a metallicity floor to the stars that form in later generations of galaxies.

Haiman et al. (2000) argued that only very low UV metagalactic background levels are required to dissociate the molecular hydrogen in haloes with masses below $10^7 - 10^8 M_\odot$. The argument was based on hydrostatic minihalo

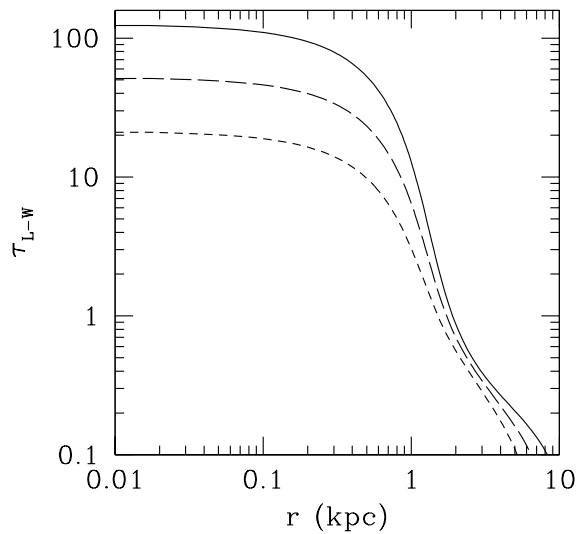


Figure 34. Optical depth of H_2 to Lyman-Werner photons in haloes collapsing at $z_c = 30$ as a function of comoving radius. Shown for haloes with initial total masses $\log(M/M_\odot) = 5.4$ (short-dashed line), 5.6 (long-dashed line) and 5.8 (solid line). The optical depth is computed inward from the turn-around radius of the halo.

models for which it was presumed that the initial molecular hydrogen content in a halo was negligible. In fact, as shown in Figure 5, substantial molecular hydrogen formation begins well before collapse, already for overdensities of only a few. A column density of $N_{H_2} \simeq 5 \times 10^{14} \text{ cm}^{-2}$ is required for self-shielding in a 1000 K halo from an external UV radiation field (Haiman et al. 2000). This is comparable to, but about a factor two larger, than the estimate of de Jong et al. (1980) for the required column density for unit optical depth due to Lyman band absorption alone, so that the optical depths shown below may be somewhat underestimated. In the model shown, for which the collapse epoch is $z_c = 20$, the molecular hydrogen column density reaches the self-shielding value by $z = 30$.

The fate of early haloes in which molecular hydrogen was formed was also neglected. These haloes will merge into larger ones, pre-enriching them in molecular hydrogen. The amount of molecular hydrogen within the turn-around radius of non-pre-enriched haloes is shown at the time of their collapse in Figure 33. This is the amount of molecular hydrogen formed in the diffuse gas retained in the halo, as distinct from molecular hydrogen that would form in the gas that becomes thermally unstable and is removed from the halo at the rate $\dot{\rho}_*$ given by Eq. (41), presumed to form stars. The open symbols correspond to the molecular hydrogen mass within haloes able to form $10^3 M_\odot$ of stars by the time they collapse. Only a small amount of molecular hydrogen need be present to reduce the cooling time sufficiently for the stars to form.

The mass in molecular hydrogen for a given halo mass is larger the earlier the collapse epoch. Approximating the optical depth to Lyman-Werner radiation as $\tau_{L-W} \simeq (N_{H_2}/5 \times$

$10^{14} \text{ cm}^{-2})(1000 \text{ K}/T)^{1/2}$, Figure 34 shows that the molecular hydrogen would be self-shielding. Further central concentration and compression in a merger event would render the molecular hydrogen even more resistant to photo-dissociation. Mergers of molecular hydrogen enriched haloes could thus build a substantial reservoir of shielded molecular hydrogen clouds within the cores of the minihaloes by the time a substantial UV background develops, lowering the minimum halo mass required for star formation.

As pre-enrichment by mergers was not considered in the models computed here, the minimum halo mass for forming a sufficient number of stars to disrupt the gas in the halo may be even smaller than the models suggest. This would further reduce the numbers of high equivalent width absorption systems along the line of sight to a bright background radio source and weaken the emission signature from minihaloes against the CMB.

6 SUMMARY AND CONCLUSIONS

A spherical collapse model is used to characterize the 21cm absorption signatures of minihaloes against bright background radio sources and the Cosmic Microwave Background prior to the Epoch of Reionization. The model evolves an initially linear spherical perturbation by simultaneously solving for the evolution of the dark matter using a shell code and the gas using a hydrodynamics code. Two sets of models, with and without molecular hydrogen formation, are computed. The ionization state of the gas is solved for as well to follow hydrogen recombinations within the halo cores. The resulting models self-consistently include inflow and an accretion shock, and match onto cosmological boundary conditions on large scales. Atomic and molecular radiative processes are included to compute the temperature structure of the haloes. A mass sink is added scaling like the local gas density and inversely with the cooling rate to avoid a thermal cooling catastrophe from developing in the halo cores in the presence of strong cooling. The mass removed is presumed to form stars.

A maximum minihalo mass for giving rise to a 21cm signal is set based on the formation of an adequate mass in stars to expel the gas from a minihalo either through photo-evaporation or a supernova-driven wind. When molecular hydrogen is allowed to form, the maximum mass at $z_c = 10$ is about $1.5 \times 10^6 M_\odot$, declining gently with the collapse epoch as $(1 + z_c)^{-1/2}$. When molecular hydrogen formation is suppressed, so that cooling is due to atomic processes alone, the maximum mass rises to $7 \times 10^6 M_\odot$ at $z = 10$, declining exponentially with redshift as $\exp[-(1 + z_c)/51]$. The central temperature of the maximum mass halo at $z = 10$ is 6500 K, well below the virial temperature of 10^4 K often assumed. The temperature is adequate for initiating the cooling required to form sufficient stars to result in the expulsion of the gas from the halo.

An inverted entropy profile near the formation of an accretion shock may produce a buoyancy instability in the infalling gas. The timescales are generally long, but could be as short as 50–100 Myr. If the gas becomes unstable to fragmentation, the details of the gas temperature and molecular hydrogen formation would be modified.

Estimates in the literature for the minimum UV radia-

tion field required to suppress molecular hydrogen formation were based on the formation of molecular hydrogen within collapsed haloes that initially had none. It is found here that haloes collapsing as early as $z_c = 30$ would form molecular hydrogen cores that were optically thick to dissociating radiation. As these systems merge into larger haloes, it is possible a substantial reservoir of self-shielded molecular hydrogen could collect in the cores of subsequent generations of haloes. In this case, the amount of star formation suppression could be less than previous estimates.

The 21cm statistical signatures are computed using a halo mass function normalized to high resolution numerical simulations. Estimates for the mass function for halo masses below the numerical resolution are made by extrapolating an extended Press-Schechter form for the mass function and an estimate based on peak statistics. Matching the two estimates for resolved haloes, the extrapolations to lower mass haloes are found to agree. The statistics are computed using the cosmological model constraints from *WMAP*, although modifications taking into account the ACT CMB data are explored as well.

Two 21cm signatures of the haloes are considered, absorption against a bright background radio source and the signature against the CMB. Two scenarios are explored, one with no large-scale galactic feedback on the IGM and one with. In the case without feedback, the IGM temperature and residual ionization following the recombination epoch are adopted for the initial linear perturbations. No further energy or external radiation field are added.

A very large number of absorption systems is produced against a bright background radio source. At $z = 8 - 10$, about 10 systems per unit redshift with an observed equivalent width $w_{v_0}^{\text{obs}}$ exceeding 0.1 kHz are predicted for the fiducial cosmological model considered. The numbers decline to a few per unit redshift for observed equivalent widths exceeding 0.25 kHz. Renormalizing to the running spectral index models constrained by both *WMAP* and ACT data decreases the counts by about 0.5-1 dex, depending on whether or not H_0 and baryonic acoustics oscillation constraints are included as well (for which the differences from the *WMAP* alone results are smaller).

Most of the features arise in haloes with masses between $10^5 - 10^6 M_\odot$. More massive haloes produce fewer absorption features both because they are fewer in number and because of their higher gas temperatures, which act to reduce the optical depth. The full mass range of the haloes that dominates the counts is beyond the reach of current cosmological numerical simulations. The results presented here indicate the mass resolution required to capture the statistics at a given equivalent width limit. Because higher mass haloes do not contribute much to systems with observed equivalent widths between 0.1 – 0.3 kHz, the statistics are fairly insensitive to the role of star formation in limiting the upper mass range of the haloes: results with and without molecular hydrogen formation yield similar results over this equivalent width range.

The observed FWHM widths of the features are typically 4 kHz, so that the absorption features would be readily resolved in frequency by currently existing or planned radio facilities capable of detecting a cosmological 21cm signal, given a sufficiently bright background source to build up the required signal to noise ratio.

The haloes have typical angular diameters of 0.05–0.25 arcsec at $z = 10$. Whilst the radio core of a quasar is smaller than this, it is unclear that the dominant radio-emitting region of a background bright radio galaxy would be. The lack of full coverage of the emitting region would reduce the number of absorbers detected. It could alter the equivalent width distribution as well. If the larger haloes giving rise to the larger equivalent width absorbers completely covered the emitting region while the smaller did not, then there would be a large relative reduction in the expected number of weaker equivalent width absorbers. The equivalent width distribution could thus serve as a probe of the size of the emitting regions of radio galaxies.

In a scenario allowing for the production of a metagalactic UV radiation field, a Ly α photon scattering rate matching the thermalization rate, required to decouple the spin temperature from the CMB temperature and begin coupling it to that of the IGM through the Wouthuysen-Field effect, produces absorption features with broad absorption wings. The equivalent width is computed relative to the wings at an observed frequency offset of 4 kHz. In some cases, mock emission lines result relative to the broad absorption wings.

In the presence of Ly α photon scattering at a rate matching or exceeding the thermalization rate P_{th} , the number of absorption features is greatly enhanced over the case with no scattering, by more than two orders of magnitude at $z = 10$ for systems with $w_{\nu_0}^{\text{obs}} > 0.15$ kHz. Increasing the Ly α photon scattering rate to $10P_{\text{th}}$, so that the spin temperature is strongly coupled to the IGM temperature everywhere, increases the number of systems with $w_{\nu_0}^{\text{obs}} > 0.25$ kHz by three orders of magnitude over the case with no scattering.

Adding a moderate amount of heat to the gas, however, substantially suppresses the number of systems. A sudden temperature boost by ten times the CMB temperature reduces the number of absorption systems with $w_{\nu_0}^{\text{obs}} > 0.2$ kHz by about 1 dex in the absence of Ly α photon scattering from the case with no temperature boost. Allowing for a Ly α photon scattering rate ten times the thermalization rate reduces the number of systems by close to a further order of magnitude.

Heating of the IGM is thus degenerate with the suppression of small scale power in terms of the number of absorption features against a bright background radio source. On the other hand, probing an unheated IGM, even if only remaining patches as sources begin to turn on, would produce an unmistakable signal of a cold IGM because of the very large number of systems that would result.

For a scenario with no large-scale galactic feedback, the minihaloes will emit relative to the CMB. The individual features have typical observed FWHM widths of 4 kHz, but are unlikely to be resolvable at the signal-to-noise levels achievable in the foreseeable future. Their collective signal, however, may be detectable. Because the strength of the signal of an individual halo increases with the mass of the halo, the overall signal is very sensitive to the assumed maximum halo mass. For models including molecular hydrogen formation, the brightness temperature differential at $z = 15$ is $\delta T_B = T_B - T_{\text{CMB}} \simeq 0.2$ mK, increasing to 0.6 mK at $z = 8$. If molecular hydrogen formation is suppressed, the increase in the upper halo mass raises the signal to 0.4 mK at $z = 15$ and 1 mK at $z = 8$. At these levels, the minihalo signal

is comparable to that of the diffuse IGM. A non-negligible contribution arises from haloes below the Jeans mass for $z > 10$.

Allowing for a running spectral index constrained jointly by the *WMAP* and ACT data suppresses the brightness temperature by about a factor of 30 at $z = 15$, and a factor of 5 at $z = 8$, without adding the constraints from H_0 and baryonic acoustic oscillation measurements. Adding these reduces the suppression factors to 8 at $z = 15$ and 2–3 at $z = 8$.

The 21cm signature against the CMB is extremely sensitive to large-scale galactic feedback. Allowing for a metagalactic UV background that produces a Ly α scattering rate as small as one percent of the thermalization rate results in an overall absorption signal from the gas within a few times the turn-around radius of the haloes. The overall signature from the minihaloes, including their environment, would be one of absorption.

The absorption signal would weaken as the IGM were heated. Once the IGM temperature exceeds the CMB temperature, however, the opposite effect occurs. Even without Ly α scattering, the emission signal from the gas beyond the core of the halo swamps the signal from within the minihalo core. Allowing for Ly α scattering further increases the strength of emission from the surrounding gas compared with that of the core.

Thus, a minimal amount of galactic feedback, either through the production of Ly α photons or through heating, results in a signal from the diffuse IGM that overwhelms that of the minihaloes. The direct measurement of a minihalo signal prior to any galactic feedback would require an absolute calibration of the brightness temperature of a radio telescope to an accuracy of better than $\delta T_B / T_{\text{CMB}} \simeq 10^{-4}$ for a detection at $z = 15$. More practical would be an experiment designed to measure the differential brightness temperature between the minihaloes and the CMB by differencing the signals from neutral and ionized patches, either in frequency or in angle on the sky. The circumstances for such a detection, however, would appear to be highly unlikely, perhaps achieved only in the earliest stages of reionisation, since the reionisation of a large fraction of the IGM would almost certainly be accompanied by galaxy or AGN produced Ly α photons, and possibly heating as well, that would be prevalent throughout the IGM (Madau et al. 1997).

APPENDIX A: MOLECULAR HYDROGEN FORMATION

A1 Reaction networks

Gas-phase molecular hydrogen production occurs principally through two catalytic processes, via the formation of the intermediaries H^- or H_2^+ :



and



Because of the low binding energy of the extra electron in H^- , the reverse of reaction Eq. (A1) induced by the Cosmic Microwave Background also becomes important at high redshifts. At high temperatures, the molecular hydrogen may be destroyed through:



Molecular hydrogen may also be destroyed through collisions with protons ($\text{H}^+ + \text{H}_2 \rightarrow \text{H}_2^+ + \text{H}^0$), but this will generally be negligible compared with Eq. (A5) in a largely neutral gas.

For primordial abundances, formation via H^- generally dominates (Palla et al. 1983; Lepp & Shull 1984). Much more extensive lists of reactions relevant to H_2 formation have been explored, including reactions with deuterium, helium and metals (Glover & Jappsen 2007), but these generally contribute negligibly to the overall abundance of H_2 created in a largely neutral diffuse medium, although they may play roles in the cooling and collapse of a molecular hydrogen cloud. Many of the rates are still poorly determined, and this may affect the rate of cooling and collapse once initiated by a sufficient abundance of molecular hydrogen (Glover & Abel 2008). Since only the formation of sufficient molecular hydrogen to drive cooling is considered here, only the H^- process is included in the halo collapse models. For the sake of completion, however, the reaction rates involving H_2^+ are listed as well.

A2 Reaction rates

The reaction chain of Eqs. (A1) and (A2) corresponds to the system

$$\frac{dn_{\text{H}^-}}{dt} = k_1 n_{\text{H}^0} n_e - (k_2 n_{\text{H}^0} + k_{51}) n_{\text{H}^-}, \quad (\text{A6})$$

$$\frac{dn_{\text{H}_2}}{dt} = k_2 n_{\text{H}^0} n_{\text{H}^-} - k_9 n_{\text{H}_2} n_{\text{H}^0}, \quad (\text{A7})$$

where n_{H^0} , n_{H^-} , n_{H_2} and n_e are the number densities of H^0 , H^- , H_2 and e^- , respectively. The reaction chain of Eqs. (A3) and (A4) corresponds to the system, including formation by H^- ,

$$\frac{dn_{\text{H}_2^+}}{dt} = k_3 n_{\text{H}^0} n_{\text{H}^+} - k_4 n_{\text{H}^0} n_{\text{H}_2^+}, \quad (\text{A8})$$

$$\frac{dn_{\text{H}_2}}{dt} = k_2 n_{\text{H}^0} n_{\text{H}^-} + k_4 n_{\text{H}^0} n_{\text{H}_2^+} - k_9 n_{\text{H}_2} n_{\text{H}^0}, \quad (\text{A9})$$

where n_{H^+} and $n_{\text{H}_2^+}$ are the number densities of H^+ and H_2^+ , respectively.

The reaction rate coefficients used are summarised in Table A1, following the labelling in Glover & Jappsen (2007). A few comments are required. The rates R1.1a and R1.1b are based on the computation of de Jong (1972), who finds

$$k_1 \simeq 8.92 \times 10^{-7} T^{-3/2} \beta(T), \quad (\text{A10})$$

where

$$\beta(T) = \int_0^k dk \frac{k^4}{(k^2 + 0.0555) \left[\exp\left(\frac{15.8k^2}{T_4}\right) - \exp\left(\frac{-0.875}{T_4}\right) \right]}, \quad (\text{A11})$$

where $T_4 = T/10^4$ K and k is the wavenumber of the electron in the reverse reaction R51 (photo-detachment). de Jong

(1972) tabulates values for k_1 over $10 < T < 15000$ K. The function $\beta(T)$ may be approximated as follows. Defining $x = T_4^{-1}$, $\beta(T) = y(x) \exp(0.875x)$, where

$$y(x) = \int_0^k dk \frac{k^4}{(k^2 + 0.0555) [\exp(15.8(k^2 + 0.0555)x) - 1]}. \quad (\text{A12})$$

Differentiating gives

$$\frac{dy}{dx} = -\frac{15.8e^{0.875x} \Gamma(5/2)}{(15.8x)^{5/2} 2e^{1.75x}} \Phi\left(e^{-0.875x}, \frac{3}{2}, 1\right), \quad (\text{A13})$$

where $\Phi(\alpha, \frac{3}{2}, 1) = \sum_{n=0}^{\infty} (n+1)^{-3/2} \alpha^n$ is a Lerch transcendental function. The resulting infinite series representation for $\beta(T)$ is resummed as a second order Padé approximant, which is the form provided in Table A1. The expression agrees with the tabulation of de Jong (1972) to better than 1 per cent for $T < 3000$ K, and to better than 4 per cent for $T < 15000$ K. In the limit $T \gg 1$, the rate approaches the asymptotic value $k_1 \sim 8.92 \times 10^{-13} \Gamma(5/2) \zeta(3/2) / [3(15.8)^{3/2}] \simeq 1.64 \times 10^{-15} \text{ cm}^3 \text{ s}^{-1}$, where ζ denotes the Riemann ζ function. This is the value given by the Padé approximant for $T \simeq 10^5$ K. An alternative rate, R1.2a and R1.2b, has been provided by Wishart (1979), which agrees reasonably well with de Jong (1972) for $T < 15000$ K, and extends the range to higher temperatures. At $T = 10^5$ K, it corresponds to $k_1 \simeq 6.34 \times 10^{-15} \text{ cm}^3 \text{ s}^{-1}$, slightly higher than the value given by R1.1a at $T = 15000$ K. For this reason R1.1a is fixed at the value at $T = 15000$ K (which agrees well with R1.2b at this temperature). The rate for R51 is based on R1.1a assuming the incident radiation is black body with a temperature T .

The laboratory measurement of rate R2 at $T = 300$ K by Martinez et al. (2009) of $k_2 \simeq 2.0 \pm 0.6 \times 10^{-9} \text{ cm}^3 \text{ s}^{-1}$ agrees very well with the theoretical value from Dalgarno & Browne (1967) (R2.1), but is also consistent with the somewhat lower value estimated by Launay et al. (1991).

Both R3.1 and R3.2 are fits to the values tabulated in Ramaker & Peek (1976). The fit R3.1 matches the tabulated values to better than 3 per cent for $100 < T < 32000$ K, decreasing in accuracy at larger values until 17 per cent too small at $T = 5 \times 10^5$ K. Between $2 < T < 30$ K the fit is as much as 50 per cent too large. The fit R3.2 matches the tabulated values to within 40 per cent over the range $10 < T < 32000$ K, and to better than 15 per cent over the range $500 < T < 8000$ K.

The rate R4.1 agrees well with the value $k_4 \simeq 6.4 \pm 1.2 \times 10^{-10} \text{ cm}^3 \text{ s}^{-1}$ measured by Karpas et al. (1979), but exceeds the alternative rate R4.2 determined by Prasad & Huntress (1980) by a factor of several.

Rate R7 has had a wide range of estimates, as recognised by Savin et al. (2004b), who argue for a similar but more definitive estimate than provided by Galli & Palla (1998), which is smaller by nearly an order of magnitude compared with the earlier cross-section rough estimate of de Jong (1972).

Rate R9.1 is a fit provided by Shapiro & Kang (1987) to the cross section values provided by Chernoff, Hollenbach & McKee in a personal communication. It is for hydrogen densities $n_{\text{H}} \ll 10^4 \text{ cm}^{-3}$ when $T < 10^4$ K. The rate R9.2 from Dove & Mandy (1986) accounts for quasi-bound states, and is valid for $n_{\text{H}} < 100 \text{ cm}^{-3}$. The rate R9.3 applies

Table A1. Gas phase reaction rate coefficients k_i (cm^3s^{-1}).

No.	Reaction	Rate coefficient	Temperature range	Ref.
R1.1a	$\text{H}^0 + \text{e}^- \rightarrow \text{H}^- + \gamma$	$1.08 \times 10^{-14} T_4 \frac{4+26z+8z^2}{4+36z+63z^2}$ $T_4 = T/10^4 \text{ K}, z = T_4/0.875$	$10 < T < 15000 \text{ K}$	1
R1.1b		4.65×10^{-15}	$T > 15000 \text{ K}$	
R1.2a		$\text{dex}(-17.845 + w(0.762 + w(0.1523 - 0.03274w)))$	$T < 6000 \text{ K}$	2
R1.2b		$\text{dex}(-16.420 + w^2(0.1998 + w^2(-0.005447 + 4.0415 \times 10^{-5}w^2)));$ $w = \log_{10} T$	$T > 6000 \text{ K}$	
R2.1	$\text{H}^0 + \text{H}^- \rightarrow \text{H}_2 + \text{e}^-$	$1.3 \times 10^{-9} (T/10^4 \text{ K})^{-0.1}$	$100 < T < 32000 \text{ K}$	3
R2.2a		1.5×10^{-9}	$T < 300 \text{ K}$	4
R2.2b		$4.0 \times 10^{-9} T^{-0.17}$	$T > 300 \text{ K}$	
R3.1	$\text{H}^0 + \text{H}^+ \rightarrow \text{H}_2^+ + \gamma$	$2.25 \times 10^{-20} \left[1 + \frac{(T/62.5)^2}{(1+T/33100)^{7/2}} \right]$	$1 < T < 10^5 \text{ K}$	5
R3.2		$\text{dex}[-19.38 + w(-1.523 + w(1.118 - 0.1269w))];$ $w = \log_{10} T$	$10 < T < 3.2 \times 10^4 \text{ K}$	5
R4.1	$\text{H} + \text{H}_2^+ \rightarrow \text{H}_2 + \text{H}^+$	5.8×10^{-10}	$T < 10^4 \text{ K}$	1
R4.2		1×10^{-10}		6
R7.1	$\text{H}^+ + \text{H}_2 \rightarrow \text{H}_2^+ + \text{H}^0$	$3 \times 10^{-10} \exp(-21050/T)$	$T < 10^4 \text{ K}$	7
R7.2		$10^{-7} f(w) \exp(-21237.15/T);$ $f(w) = -3.3232183 + w(3.3735382 + w(-1.4491368 +$ $w(0.34172805 + w(-0.047813720 +$ $w(0.0039731542 + w(-0.00018171411 + 3.5311932 \times 10^{-6}w)))));$ $w = \log(T)$	$100 < T < 3 \times 10^4 \text{ K}$	8
R9.1	$\text{H}^0 + \text{H}_2 \rightarrow 3\text{H}^0$	$1.12 \times 10^{-10} \exp(-70350/T)$		9
R9.2		$8.04 \times 10^{-11} T_4^{2.012} \exp(-51790/T)/(1 + 0.2130T_4)^{3.512};$ $T_4 = T/10^4 \text{ K}$	$10^3 < T < 10^5 \text{ K}$	10
R9.3		$6.67 \times 10^{-12} T^{1/2} / \exp(1 + 63590/T)$		11
R51	$\text{H}^- + \gamma \rightarrow \text{H}^0 + \text{e}^-$	$1.04 \times 10^8 T_4^{5/2} \frac{4+26z+8z^2}{4+36z+63z^2} \exp(-1/z)$ $1.62 \times 10^8 T_4^{1.5} \exp(-1/z)$ $T_4 = T/10^4 \text{ K}, z = T_4/0.875$	$10 < T < 10^4 \text{ K}$ $T > 10^4 \text{ K}$	1

REFERENCES: (1) de Jong (1972); (2) Wishart (1979); (3) Dalgarno & Browne (1967); (4) Launay et al. (1991); (5) Ramaker & Peek (1976); (6) Prasad & Huntress (1980); (7) Galli & Palla (1998); (8) Savin et al. (2004b,a); (9) Shapiro & Kang (1987); (10) Dove & Mandy (1986); (11) Mac Low & Shull (1986)

in the low density limit $n_{\text{H}} < 1 \text{ cm}^{-3}$ (Lepp & Shull 1983; Mac Low & Shull 1986).

The computations for this paper generally used rates R1.1a, R2.1, R9.2 and R51, although comparison runs were made using some of the alternative rates. The results were not found very sensitive to the choices.

A3 Numerical integration scheme

Despite its simplicity, the system Eqs. (A6) and (A7) is not straightforward to solve numerically because of the discrepant timescales between the formation of H^- and H_2 , rendering the system stiff. The solution to the system is

$$n_{\text{H}^-}(t) = n_{\text{H}^-, \text{eq}}(t) + [n_{\text{H}^-}(0) - n_{\text{H}^-, \text{eq}}(0)] \times \exp \left[- \int_0^t dt' (k_2(t') n_{\text{H}^0}(t') + k_{51}(t')) \right]; \quad (\text{A14})$$

$$n_{\text{H}_2}(t) = n_{\text{H}_2}(0) \exp \left[- \int_0^t dt' k_9(t') n_{\text{H}^0}(t') \right] + \exp \left[- \int_0^t dt' k_9(t') n_{\text{H}^0}(t') \right] \times \int_0^t dt' \exp \left[- \int_0^{t'} dt'' k_9(t'') n_{\text{H}^0}(t'') \right] \times [k_2(t') n_{\text{H}^0}(t') n_{\text{H}^-}(t')], \quad (\text{A15})$$

where $n_{\text{H}^-, \text{eq}}(t) = k_1(t) n_{\text{H}^0}(t) n_e(t) / [k_2(t) n_{\text{H}^0}(t) + k_{51}(t)]$ is the equilibrium number density of n_{H^-} , which is rapidly achieved at high redshifts on the timescale $1/(k_2 n_{\text{H}^0} + k_{51})$.

For solving the equations in a homogeneous expanding universe, it is useful to recast them as

$$\frac{dx_{\text{H}^-}}{d\tau} = f_{10} - d_{11} x_{\text{H}_2}; \quad (\text{A16})$$

$$\frac{dx_{\text{H}_2}}{d\tau} = f_{21} x_{\text{H}^-} - d_{22} x_{\text{H}_2}, \quad (\text{A17})$$

where $x_{\text{H}^-} = n_{\text{H}^-} / n_{\text{H, Tot}}$, $x_{\text{H}_2} = n_{\text{H}_2} / n_{\text{H, Tot}}$, with $n_{\text{H, Tot}}$ indicating the total density of hydrogen nuclei in all species, $f_{10} = k_1 n_e x_{\text{H}^0} / H(a)$, with $x_{\text{H}^0} = n_{\text{H}^0} / n_{\text{H, Tot}}$, $d_{11} = (k_2 n_{\text{H}^0} + k_{51}) / H(a)$, $f_{21} = k_2 n_{\text{H}^0} / H(a)$, $d_{22} = k_9 n_{\text{H}^0} / H(a)$, $H(a)$ is the Hubble constant at epoch $a = 1/(1+z)$, and $\tau = \log a$. The rapidity with which H^- reaches its equilibrium value suggests the following second-order accurate scheme

$$x_{\text{H}^-}^{n+1} = x_{\text{H}^-, \text{eq}}^{n+1} + (x_{\text{H}^-}^n - x_{\text{H}^-, \text{eq}}^n) \times \exp \left[- \frac{1}{2} (d_{11}^{n+1} + d_{11}^n) \Delta\tau \right]; \quad (\text{A18})$$

$$x_{\text{H}_2}^{n+1} = x_{\text{H}_2}^n \exp \left[- \frac{1}{2} (d_{22}^{n+1} + d_{22}^n) \Delta\tau \right]$$

$$\begin{aligned}
 & + \frac{1}{2} \left\{ f_{21}^n x_{\text{H}^-}^n \exp \left[-\frac{1}{2} (d_{22}^{n+1} + d_{22}^n) \Delta\tau \right] \right. \\
 & \left. + f_{21}^{n+1} x_{\text{H}^-}^{n+1} \right\} \Delta\tau \quad (\text{A19})
 \end{aligned}$$

for advancing the abundance fractions from time step τ^n to $\tau^{n+1} = \tau^n + \Delta\tau$.

REFERENCES

- Abel T., Bryan G. L., Norman M. L., 2000, *ApJ*, 540, 39
- Allison A. C., Dalgarno A., 1969, *ApJ*, 158, 423
- Balbus S. A., Soker N., 1989, *ApJ*, 341, 611
- Bardeen J. M., Bond J. R., Kaiser N., Szalay A. S., 1986, *ApJ*, 304, 15
- Bertschinger E., 1985, *ApJS*, 58, 39
- Bhattacharya S., Heitmann K., White M., Lukić Z., Wagner C., Habib S., 2010, *ArXiv e-prints*, 1005.2239
- Blumenthal G. R., Faber S. M., Primack J. R., Rees M. J., 1984, *Nat.*, 311, 517
- Blumenthal G. R., Faber S. M., Primack J. R., Rees M. J., 1985, *Nat.*, 313, 72
- Bond J. R., Cole S., Efstathiou G., Kaiser N., 1991, *ApJ*, 379, 440
- Bond J. R., Myers S. T., 1996a, *ApJS*, 103, 1
- Bond J. R., Myers S. T., 1996b, *ApJS*, 103, 63
- Bond J. R., Szalay A. S., 1983, *ApJ*, 274, 443
- Bond J. R., Szalay A. S., Silk J., 1988, *ApJ*, 324, 627
- Carilli C. L., Gnedin N. Y., Owen F., 2002, *ApJ*, 577, 22
- Couchman H. M. P., Rees M. J., 1986, *MNRAS*, 221, 53
- Dalgarno A., Browne J. C., 1967, *ApJ*, 149, 231
- de Jong T., 1972, *A&Ap*, 20, 263
- de Jong T., Boland W., Dalgarno A., 1980, *A&Ap*, 91, 68
- Dekel A., Rees M. J., 1987, *Nat.*, 326, 455
- Dove J. E., Mandy M. E., 1986, *ApJ*, 311, L93
- Dunkley J., Hlozek R., Sievers J., Acquaviva V., Ade P. A. R., Aguirre P., Amiri M., Appel J. W., Barrientos L. F., Battistelli E. S., Bond J. R., Brown B., Burger B., Chervenak J., Das S., Devlin M. J., 2010, *ArXiv e-prints*, 1009.0866
- Field G. B., 1958, *Proc. I.R.E.*, 46, 240
- Field G. B., 1959a, *ApJ*, 129, 536
- Field G. B., 1959b, *ApJ*, 129, 551
- Fillmore J. A., Goldreich P., 1984, *ApJ*, 281, 1
- Fuller T. M., Couchman H. M. P., 2000, *ApJ*, 544, 6
- Furlanetto S. R., Loeb A., 2002, *ApJ*, 579, 1
- Furlanetto S. R., Loeb A., 2004, *ApJ*, 611, 642
- Galli D., Palla F., 1998, *A&Ap*, 335, 403
- Gamow G., 1948, *Physical Review*, 74, 505
- Glover S. C. O., Abel T., 2008, *MNRAS*, 388, 1627
- Glover S. C. O., Brand P. W. J. L., 2001, *MNRAS*, 321, 385
- Glover S. C. O., Jappsen A., 2007, *ApJ*, 666, 1
- Gnedin N. Y., 2010, *ApJ*, 721, L79
- Haiman Z., Abel T., Rees M. J., 2000, *ApJ*, 534, 11
- Haiman Z., Rees M. J., Loeb A., 1997a, *ApJ*, 476, 458
- Haiman Z., Rees M. J., Loeb A., 1997b, *ApJ*, 484, 985
- Hirasawa T., 1969, *Progress of Theoretical Physics*, 42, 523
- Hogan C. J., Rees M. J., 1979, *MNRAS*, 188, 791
- Ikeuchi S., 1986, *ApSS*, 118, 509
- Iliev I. T., Shapiro P. R., Ferrara A., Martel H., 2002, *ApJ*, 572, L123
- Jelić V., Zaroubi S., Labropoulos P., Thomas R. M., Bernardi G., Brentjens M. A., de Bruyn A. G., Ciardi B., Harker G., Koopmans L. V. E., Pandey V. N., Schaye J., Yatawatta S., 2008, *MNRAS*, 389, 1319
- Karpas Z., Anicich V., Huntress W. T., 1979, *J.Chem.Phys.*, 70, 2877
- Komatsu E., Dunkley J., Nolta M. R., Bennett C. L., Gold B., Hinshaw G., Jarosik N., Larson D., Limon M., Page L., Spergel D. N., Halpern M., Hill R. S., Kogut A., Meyer S. S., Tucker G. S., Weiland J. L., Wollack E., Wright E. L., 2009, *ApJS*, 180, 330
- Komatsu E., Smith K. M., Dunkley J., Bennett C. L., Gold B., Hinshaw G., Jarosik N., Larson D., Nolta M. R., Page L., Spergel D. N., Halpern M., Hill R. S., Kogut A., Limon M., Meyer S. S., 2010, *ArXiv e-prints*
- Kuhlen M., Madau P., Montgomery R., 2006, *ApJ*, 637, L1
- Launay J. M., Le Dourneuf M., Zeppen C. J., 1991, *A&Ap*, 252, 842
- Leitherer C., Schaerer D., Goldader J. D., González Delgado R. M., Robert C., Kune D. F., de Mello D. F., Devost D., Heckman T. M., 1999, *ApJS*, 123, 3
- Lepp S., Shull J. M., 1983, *ApJ*, 270, 578
- Lepp S., Shull J. M., 1984, *ApJ*, 280, 465
- Mac Low M., Shull J. M., 1986, *ApJ*, 302, 585
- Machacek M. E., Bryan G. L., Abel T., 2001, *ApJ*, 548, 509
- Madau P., Meiksin A., Rees M. J., 1997, *ApJ*, 475, 429
- Malagoli A., Rosner R., Bodo G., 1987, *ApJ*, 319, 632
- Martinez O., Yang Z., Betts N. B., Snow T. P., Bierbaum V. M., 2009, *ApJ*, 705, L172
- Meiksin A., 1988, *ApJ*, 334, 59
- Meiksin A., 1994, *ApJ*, 431, 109
- Meiksin A., 2006, *MNRAS*, 370, 2025
- Meiksin A., 2010, *MNRAS*, 402, 1780
- Meiksin A. A., 2009, *Reviews of Modern Physics*, 81, 1405
- Mesinger A., Bryan G. L., Haiman Z., 2009, *MNRAS*, 399, 1650
- Morales M. F., Bowman J. D., Hewitt J. N., 2006, *ApJ*, 648, 767, *arXiv:astro-ph/0510027*
- Oh S. P., Mack K. J., 2003, *MNRAS*, 346, 871
- Omukai K., Nishi R., 1999, *ApJ*, 518, 64
- O'Shea B. W., Abel T., Whalen D., Norman M. L., 2005, *ApJ*, 628, L5
- Ostriker J. P., Gnedin N. Y., 1996, *ApJ*, 472, L63
- Palla F., Salpeter E. E., Stahler S. W., 1983, *ApJ*, 271, 632
- Peebles P. J. E., 1980, *The large-scale structure of the universe*. Princeton University Press, Princeton, NJ
- Peebles P. J. E., 1984, *ApJ*, 277, 470
- Peebles P. J. E., Dicke R. H., 1968, *ApJ*, 154, 891
- Prasad S. S., Huntress Jr. W. T., 1980, *ApJS*, 43, 1
- Press W. H., Schechter P., 1974, *ApJ*, 187, 425
- Ramaker D. E., Peek J. M., 1976, *Phys. Rev. A*, 13, 58
- Reed D. S., Bower R., Frenk C. S., Gao L., Jenkins A., Theuns T., White S. D. M., 2005, *MNRAS*, 363, 393
- Reed D. S., Bower R., Frenk C. S., Jenkins A., Theuns T., 2007, *MNRAS*, 374, 2
- Rees M. J., 1986, *MNRAS*, 218, 25P
- Saslaw W. C., Zipoy D., 1967, *Nat.*, 216, 976

- Savin D. W., Krstić P. S., Haiman Z., Stancil P. C., 2004a, ApJ, 607, L147
- Savin D. W., Krstić P. S., Haiman Z., Stancil P. C., 2004b, ApJ, 606, L167
- Scott D., Rees M. J., 1990, MNRAS, 247, 510
- Seager S., Sasselov D. D., Scott D., 2000, ApJS, 128, 407, arXiv:astro-ph/9912182
- Shapiro P. R., Ahn K., Alvarez M. A., Iliev I. T., Martel H., Ryu D., 2006, ApJ, 646, 681
- Shapiro P. R., Kang H., 1987, ApJ, 318, 32
- Shaver P. A., Windhorst R. A., Madau P., de Bruyn A. G., 1999, A&Ap, 345, 380
- Tozzi P., Madau P., Meiksin A., Rees M. J., 2000, ApJ, 528, 597
- Whalen D., Hueckstaedt R. M., McConkie T. O., 2010, ApJ, 712, 101
- Whalen D., O'Shea B. W., Smidt J., Norman M. L., 2008, ApJ, 679, 925
- Wise J. H., Abel T., 2007, ApJ, 671, 1559
- Wishart A. W., 1979, MNRAS, 187, 59P
- Wouthuysen S. A., 1952, AJ, 57, 31
- Yoshida N., Oh S. P., Kitayama T., Hernquist L., 2007, ApJ, 663, 687
- Yue B., Ciardi B., Scannapieco E., Chen X., 2009, MNRAS, 398, 2122
- Zygelman B., 2005, ApJ, 622, 1356